1 **Enhancing the self-sensing and energy storage capabilities of cementitious composites**
2 **through marine sand doping**

3 Thamer Almotlaq[a,b], Bo Huang[c*], Mohamed Saafi[a*], Jianqiao Ye[a]
4 [a]School of Engineering, Lancaster University, Lancaster, LA1 4YR, UK
5 [b]Civil Engineering department, College of Engineering, Jouf University, Sakaka 72388,
6 Saudi Arabia
7 [c]School of Civil Engineering, Hunan University of Science and Technology, Xiangtan,
8 411201, China

9 **Abstract**

10 In this paper, for the first time, we investigate the inherent ionic conductivity of seawater-based

11 cementitious composites containing marine sand aggregates, when air cured over 28 days with

12 the objective of uncovering new functionalities. Electrochemical impedance spectroscopy

13 (EIS), cyclic voltammetry (CV) and density functional theory (DFT) were employed to

14 elucidate the ionic conduction mechanisms in this material system and characterize its stress

15 self-sensing and electrochemical charge retention capabilities. The results revealed that the

16 marine aggregates are not ionic conductive materials; however, they facilitate improved

17 electrochemical response through enhanced formation of highly ion-exchanging calcium-

18 silicate-hydrate (C-S-H) phases, coupled with integrated porous channels that enable sustained

19 ion mobility despite drying. This synergistic ion transport yielded a bulk ionic resistivity

20 around 25 kΩ.cm at room temperature, which lies in typical ranges seen in solid-state

21 electrolytes for battery systems. Controlled compressive loading indicates appreciable self-

22 sensing capacity at low-stress levels, suggesting applicability to detect the onset of mechanical

23 damage. Negligible charge leakage upon 28 days of curing further demonstrates the electrical

24 energy storage potential of the sea-based cement. By harnessing locally available seawater and

25 marine sand resources to develop ionic conductive cementitious composites, this work provides

26 the framework to optimize durable multifunctionality for sensing and electrical energy storage

27 in reinforced concrete infrastructure. This in return improves the sustainability and energy

28 efficiency of the built environment.

29 * Corresponding authors. Email address: m.saafi@lancaster.ac.uk (M.Saafi), t.almotlaq@lancaster.ac.uk (T. Almotlaq)
30 bohuang@hnust.edu.cn (B. Huang),

1.   Introduction

Concrete is the most widely used manmade material with an annual production exceeding 25 billion tons globally [1]. The development of multifunctional concretes that exhibit electrical conductivity alongside mechanical properties, opens the door to various sustainable and smart infrastructure applications [2–4]. These applications include self-sensing for structural health monitoring [5,6], thermal and electrical energy storage [7,8], electromagnetic interference shielding [9], and road deicing [10].

However, conventional cementitious composites exhibit inherently high electrical resistivity [11,12]. To introduce electrical conductivity, highly conductive nanomaterials such as carbon nanofibers [13], carbon nanotubes [14], and graphene nanoplatelets [15] are incorporated into cementitious matrices. The significant difference in chemical properties, however, presents challenges in achieving efficient production of cementitious composites, often leading to non-uniform dispersion, agglomeration, and poor interfacial bonding between the matrix and conductive fillers [16]. Another major obstacle to the widespread utilization of conductive additives in concretes is their high costs and energy-intensive production methods, leading to increased embodied carbon in concrete. The global annual production of advanced nano-additives remains low [17]. Scaling up manufacturing processes for these materials for applications in construction requires high-temperature reactors, leading to high energy consumption and carbon dioxide (CO_2) emissions. As a result, the addition of conductive fillers to concrete is expected to increase the overall CO_2 footprint compared to plain concrete.

The high electrical conductivity achieved by incorporating conductive additives is typically measured under saturated conditions, and it tends to decrease significantly as the cementitious materials undergo moisture loss. Recent studies have shown a significant drop in the electrical conductivity of conductive cementitious composites, ranging from 60-80%, after standard air curing following an initial 28-day moist curing period [18- 21]. The initial high conductivity

56 during moist curing comes from the ionic species in the pore solution. However, as

57 cementitious composites undergo hydration and subsequent air exposure, internal moisture

58 content decreases over time. This reduces the pore solution crucial for ion mobility. In the

59 absence of enough protons (H^+) and hydroxyl (OH^-) ions from water, the primary charge

60 transport shifts to electron tunneling mode, requiring direct contacts between adjacent

61 conductive fillers [22, 23]. However, the complete loss of moisture increases the tunneling

62 distances between the disconnected conductive fillers, leading to the loss of efficient

63 conductive networks [22, 23]. This limitation poses a challenge in concrete structures where

64 consistent conductivity is essential for self-sensing, energy storage, or electromagnetic

65 shielding functionalities.

66 The challenges mentioned above highlight the need for alternative cementitious systems that

67 exhibit inherent stable functionality over time, unaffected by moisture loss and without relying

68 on added conductive fillers.

69 Recent studies have explored the use of seawater in place of regular fresh water to produce

70 cementitious materials. Experimental results demonstrated that the microstructure and

71 mechanical performance of seawater-blended composites exhibit notable improvements over

72 those of traditional counterparts. This arises from the accelerated precipitation of additional

73 calcium-silicate-hydrate (C-S-H) gel phases that refine pores and densify the cement matrix

74 because of the abundant ions in the seawater [24, 25]. This approach aligns well with

75 sustainable construction principles, as leveraging seawater eliminates usage of limited

76 freshwater reserves for concrete production [26].

77 In this paper, we argue that cementitious composites synthesized with seawater and marine

78 sand aggregates, when air cured, can demonstrate stable ionic conductivity that can be

79 exploited for low-stress self-sensing and electrical energy storage functionalities. To

80 substantiate this premise, we first electrochemically characterize cement pastes with seawater

81 (C-SW) and those also supplemented with sea sand (C-SW-SS) to quantify and compare their

82 ionic conductivity and elucidate the underlying conduction mechanisms for the purpose of

83 evaluating the effects of additional sea sand on ion the transport properties. Controlled

84 mechanical loading tests are then performed on the C-SW-SS composite to assess its self-

85 sensing capacity through measured variations in electrical impedance with applied compressive

86 stress. Cyclic voltammetry (CV) studies further probe the ability of the C-SW-SS composite to

87 retain electrochemical charges for potential energy storage.

88 **2. Methodology**

89 2.1. *Materials and sample preparation*

90 Ordinary Portland cement (OPC) consisting of CEM 1 was used as a binder. Sea sand (SS) and

91 seawater (SW), collected from the Lancashire coast, UK, were used as fillers and mixing liquid.

92 The chemical composition of OPC is given in Table 1 whereas the ionic compounds found in

93 the seawater are given Table 2 [27]. The SW/OPC and SS/OPC ratios were 0.5 and 3,

94 respectively. Cement pastes were prepared to cast 48 cubes (40 mm x 40 mm x 40 mm) for

95 electrochemical characterization: 24 cubes made of OPC, SW and SS (C-SW-SS) and 24 cubes

96 made of OPC and SW (C-SW) were used for comparison purposes. The C-SW and C-SW-SS

97 mix proportions are given in Table 3.

98 Additionally, 12 C-SW-SS prisms (40 mm x 40 mm x 160 mm) and 12 C-SW-SS plates (5 mm

99 x 25 mm x 80 mm) plates were used for piezoresistive and electrochemical charge retention

100 characterization, respectively.

101 After wet mixing, the pastes were poured into the cube and prism molds and two electrodes

102 were inserted for electrochemical and piezoresistive characterization. Two stainless steel

103 electrodes were embedded in the cubes with a distance of 35 mm and a contact area of 900

104 mm^2 and two stainless steel electrodes were embedded into the prisms with a distance between

105 them of 120 mm and a contact area of 900 mm^2. After 24 hours for curing, the prisms and the

cubes were demolded and left to cure in air at room temperature until electrochemical impedance spectroscopy (EIS) and piezoresistive characterization. To prepare the C-SW-SS plates, the pastes were sandwiched between two porous carbon felt electrodes and left to cure in air at room temperature until cyclic voltammetry (CV) characterization. This commercially available carbon felt is commonly used in electrochemical capacitors and batteries due to its high specific surface area and electrically conductive framework. It stores charge electrostatically via reversible ion adsorption at the electrode-electrolyte interface within its intricately interconnected pore structure.

Table 1: Chemical composition of OPC.

Chemical Element	By mass (%)
SiO_2	20.38
Al_2O_3	5.4
Fe_2O_3	2.82
CaO	63.04
MgO	1.74
Loss of ignition	1.66

Table 2: Chemical compounds of seawater.

Compound	Amount (mg/L)
Na^+	12200
K^+	500
Ca^{2+}	430
Mg^{2+}	1110
Cl^-	16550
SO_4^{2-}	2220

Table 3: Mix proportions of mortars

Ingredient (g/L)	C-SW	C-SW-SS
OPC	720	720
SW	360	360
SS	-	1080
W/C	0.5	0.5

2.2.   *Microstructure and EIS characterization of C-SW and C-SW-SS composites*

Scanning Electron Microscopy (SEM) fitted with an X-ray Energy Dispersive Spectrometer (EDS) (JSM-7800F) was employed to quantify the morphology and elemental mapping in the sea sand and cementitious composites at 28 days of air curing. The EIS method was utilized to study the electrochemical behavior of the C-SW and C-SW-SS composites. The Potentiostat (Gamry Interface 1010E) was used to conduct EIS measurements by applying a sinusoidal voltage of 10 mV with a frequency scan in the range of 0.1 Hz to 1 MHz through the two stainless steel mesh electrodes using the two-probe method shown in Fig. 1a.

126 The EIS results were analyzed using Gamry software[TM] to unveil the primary mechanisms

127 governing the electrical conduction and ion transport within the cementitious composites. The

128 bulk ionic electrical resistance of the C-SW and C-SW-SS cubes was calculated following the

129 method described in [28]. In this approach, the bulk electrical resistance was determined from

130 the Bode plot of the impedance modulus log|Z| and phase, as illustrated in Fig. 1b. In this figure,

131 the bottom rectangle demonstrates the phase plateauing near zero in the high-frequency range,

132 while the top rectangle shows log|Z| values in this frequency range where the phase is

133 plateauing near zero. In this frequency range, the cementitious composites exhibit resistive

134 behavior, and their bulk ionic resistance can be calculated from the average log|Z| values as R

135 $(\Omega) = 10^{\wedge}\log|Z|$ [28].
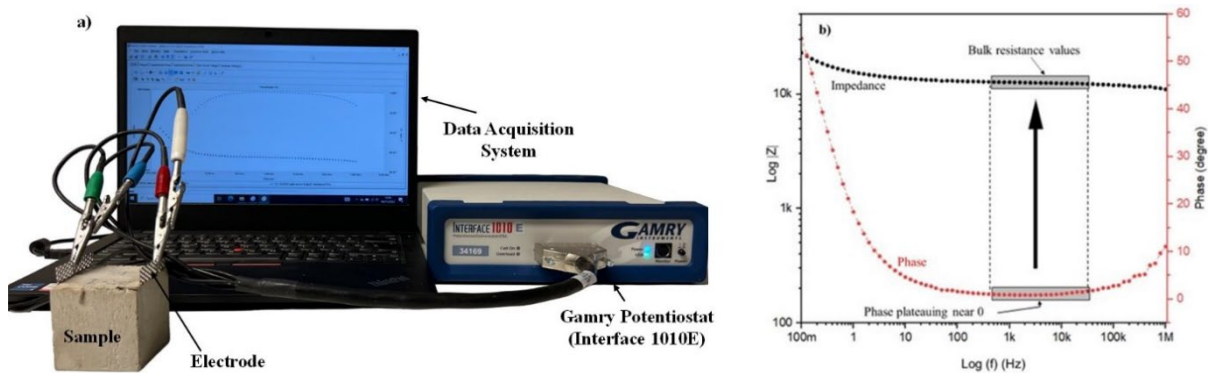
136

137 Figure 1. Electrochemical characterization setup and method for ionic resistance calculation.

138 *2.3.   Characterization of multifunctionality of C-SW-SS composite*

139 Figure 2a illustrates the experimental setup used to characterize the piezoresistive behavior of

140 the C-SW-SS prisms subjected to a monotonic compressive load from 0 to 20 kN with a

141 displacement rate of 0.05 mm/min. At each load step, the impedance of the prisms was

142 measured using the Gamry Potentiostat, following the same procedure as in the aforementioned

143 EIS characterization. And the change in the real impedance as a function of the compressive

144 stress was established.

145   The electrochemical charge retention capability of C-SW-SS was further elucidated through

146   cyclic voltammetry characterization, utilizing the setup depicted in Fig. 2b. In this test, an

147   electrical current was passed through the sample via the carbon felt electrodes while the voltage

148   was swept between -1 V and +1 V by employing scan rates ranging from 50 to 300 mV/s. The

149   shape of the resulting current vs voltage spectra was examined to assess the C-SW-SS

150   composite's ability to retain charge. These spectra offer crucial visual insights into determining

151   whether the C-SW-SS demonstrates promising electrochemical charge storage behavior for use

152   in batteries and capacitors. Elliptical, rectangular, and leaf-like CV shapes serve as indicators

153   of charge-retaining capability.
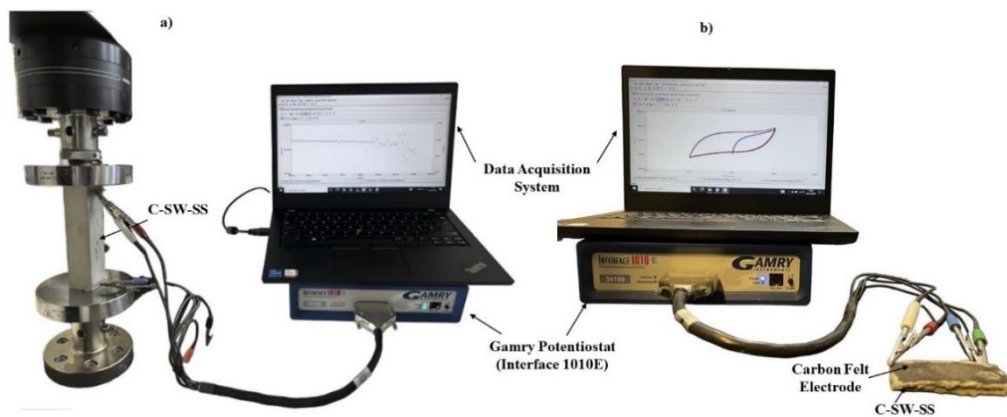
155   Figure 2. Characterization of multifunctional properties of C-SW-SS. a) self-stress sensing, b)
156   electrochemical charge retention capacity.

157   *2.4.   Computed band structure analysis of sea sand*

158   Utilizing an open-source density functional theory (DFT) computations [29], the electronic

159   structure properties were explored for the alkali metal minerals inherently present in the sea

160   sand compositions. Calculated band gap energies exceeding 2 eV coupled with ion migration

161   activation barriers more than 1 eV indicate non-ionic-conductive materials. Consequently, the

162   inherent ionic conductivity of the sea sand is negligible.

163

164   **3.   Experimental Results**

165   *3.1.   Crystal structure and electronic properties of sea sand*

166 To elucidate whether the sea sand particles contribute to the overall ionic conductivity of the

167 C-SW-SS cement composite, their morphology, crystal structure, and electronic properties

168 were determined. Figure 3 displays the SEM and EDX elemental analysis, while Fig. 4 presents

169 EDX elemental mapping, all conducted in the same location on the sea sand particle. As

170 demonstrated in Figures 3a-b, the sea sand exhibits a porous and spongy texture, marked by

171 countless uniformly distributed tiny openings. The surface resembles a sponge, featuring

172 numerous pores that are somewhat interconnected, creating a highly porous structure. These

173 openings enhance the sand's ability to interact with sea water, allowing for efficient absorption

174 and release. This observation aligns seamlessly with the conclusions drawn from prior studies,

175 highlighting the sea sand's inherent porous nature with a pore volume surpassing 30% [30, 31].

176 This prevailing characteristic of porosity in the sea sand is expected to contribute to ion

177 diffusion within the C-SW-SS composite. The EDX elemental analysis of the sea sand (inset

178 in Fig. 3d) is presented in Fig. 3c.

179 Sea sand and ordinary sand exhibit distinct chemical compositions. The sea sand is primarily

180 composed of approximately 21% silica (Si), 20.8% carbon (C), 2.4% aluminum (Al), and

181 52.3% oxygen (O). In contrast, ordinary sand, with its well-established composition, consists

182 predominantly of around 53% silica (Si) and 45% oxygen (O), with traces of calcium (Ca) and

183 aluminum (Al) comprising about 2%. Notably, the sea sand contains ionic species such as

184 potassium (K^+), sodium (Na^+), and magnesium (Mg^{2+}), with concentrations of 1%, 0.8%, and

185 0.2%, respectively. Additionally, calcium (Ca) is present in both ionic and covalently bound

186 forms in sea sand, with a concentration of 0.5%. Conversely, ordinary sand does not contain

187 ionic species like the sea sand. Elemental mapping images illustrating the distribution of K^+,

188 Na^+, Mg^{2+} and Ca are provided in Figs. 4a-d. It is evident that, except for Ca, all other ionic

189 species exhibit a uniform distribution within the SS particle.

190
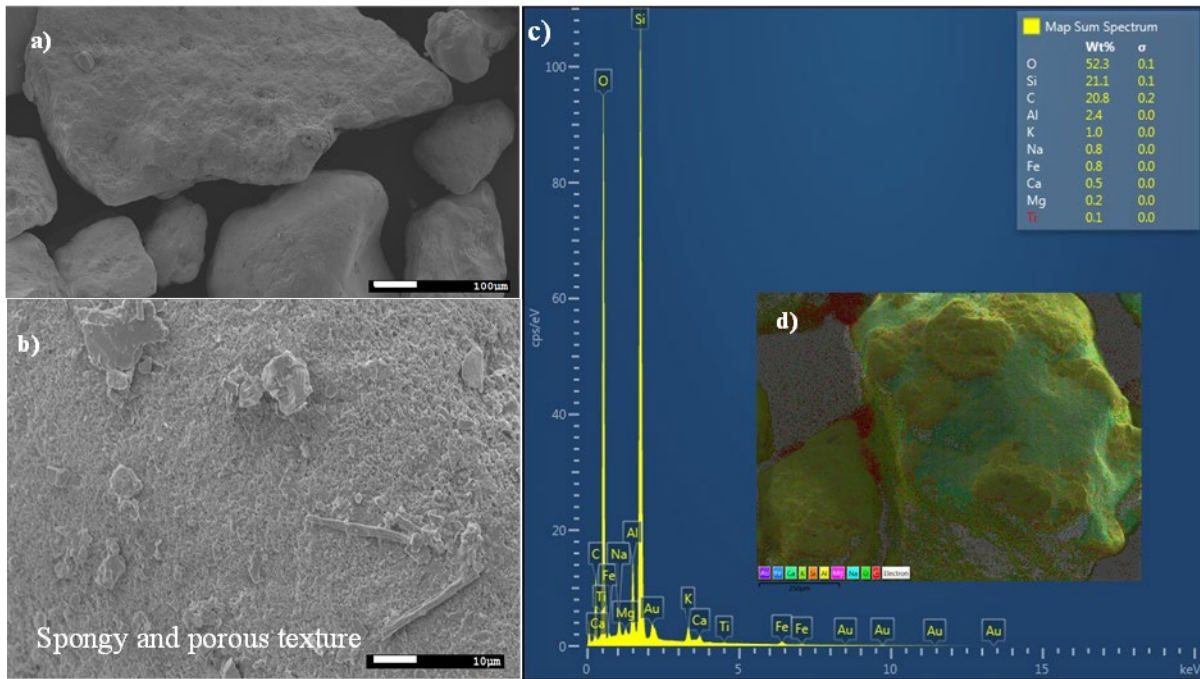
Figure 3. SEM and EDX elemental analysis of sea sand. a) SEM image, b) SEM image showing sea sand exhibiting a porous and spongy texture, c) EDX spectrum of the sea sand shown in inset d).

Further XRD analysis was conducted to investigate the mineralogical composition of the sea sand. The XRD spectrum presented in Fig. 5 reveals the predominant minerals as quartz (SiO_2), leucite ($KAlSi_2O_6$), albite ($NaAlSi_3O_8$), calcite ($CaCO_3$), garnet ($Al_2Fe_3(SiO_4)_3$), and traces of dolomite ($CaMg(CO_3)_2$) and rutile (TiO_2). Additionally, carbon (C) was detected in the sample. Of particular interest among the identified minerals are the K and Na-bearing minerals ($KAlSi_2O_6$ and $NaAlSi_3O_8$), as they have the potential to contribute to the overall ionic conductivity of the C-SW-SS composite due to the presence of K^+ and Na^+ ions. The activation energy (E_a) of these K^+ and Na^+-bearing minerals can provide insights into whether they exhibit ionic conducting or insulating properties. Activation energy (E_a) represents the energy barrier that ions must overcome to move between sites. Typically, the activation energy of ionic conductors falls within the range of 0.1-1 eV [32].
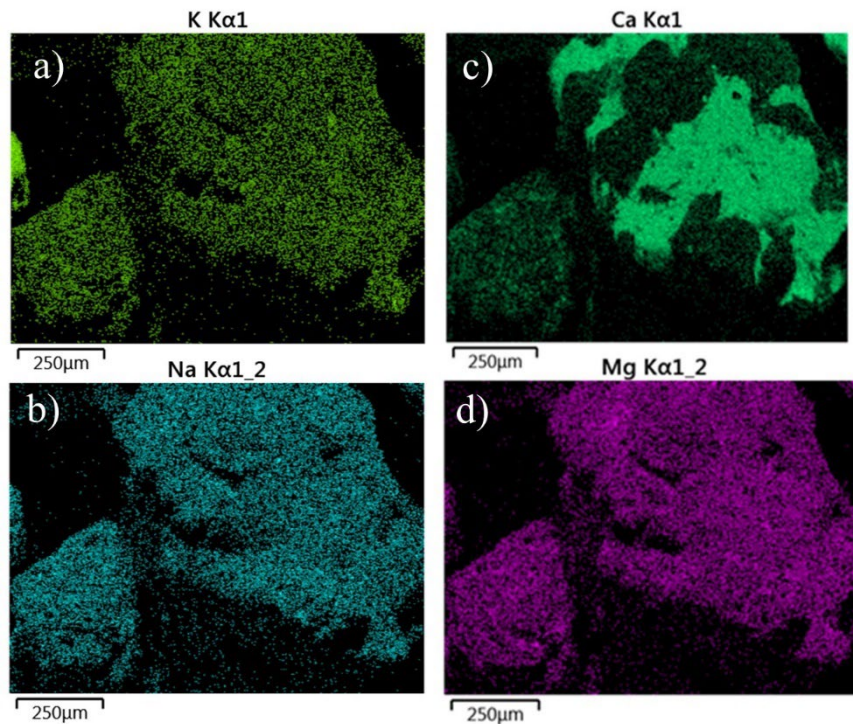
Figure 4. EDX elemental mapping images. a) K element map, d) Na element map, e) Ca element map, f) Mg element map.

As illustrated in Figs. 5b-c, the structure of the $KAlSi_2O_6$ and $NaAlSi_3O_8$ minerals, characterized by a $[SiO_4/AlO_4]$ tectosilicate 3D network, was employed for the computation of their energy band structure using DFT.

The energy band structure diagram of sea sand is depicted in Fig. 6. This diagram illustrates the distribution of energy levels for electrons in the crystalline phase of sea sand. Essentially, it provides insights into the behavior of electrons and their mobility within the sea sand, determining whether it exhibits ionic conductivity or behaves as an insulator.

The energy band structure diagram of sea sand, as shown in Fig. 6, is divided into three main bands. The valence band, represented by the bottom section of the energy band diagram, is the highest occupied energy band in the ground state of sea sand. In this band, electrons are tightly bound to individual atoms and are not free to move throughout its crystal phases. On the other hand, the conduction band, represented by the top section of the band energy diagram, is the lowest unoccupied energy band where electrons are free to move throughout the crystal phases of sea sand, contributing to ionic conduction.

The energy band gap (E_g) is defined as the energy between the top of the valence band and the bottom of the conduction band. This energy is required for electrons to transition from the valence band to the conduction band, enabling the formation of current. The calculated energy band gap (E_g) is 4.75 eV and 4.45 eV for $KAlSi_2O_6$ and $NaAlSi_3O_8$, respectively. These high band gaps indicate a low propensity for ionic conductivity in these minerals due to the substantial energy barrier that ions must overcome to transition from the valence band to the conduction band and contribute to ionic conduction. Consequently, their contribution to the overall ionic conductivity of the C-SW-SS composite is negligible.
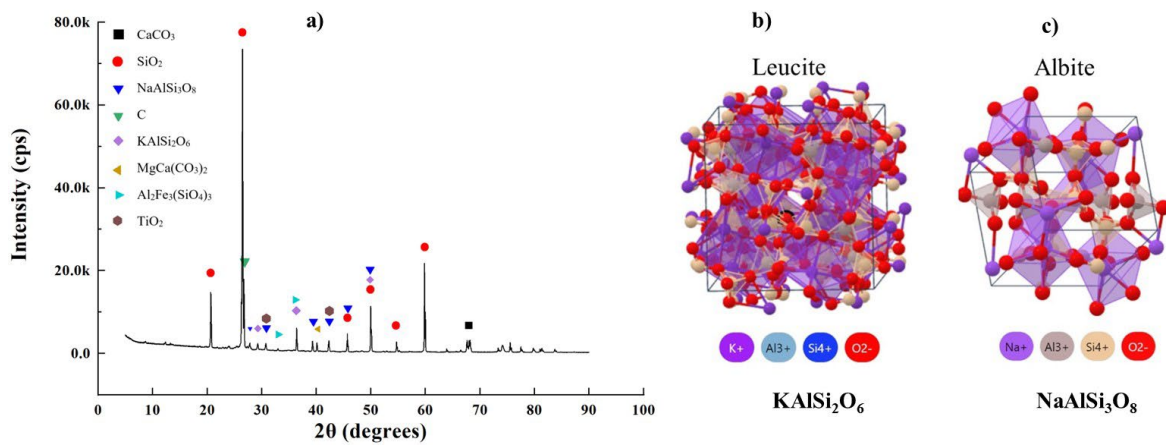
Figure 5. Crystal structure of sea sand. a) XRD spectrum of the SS particles, b) lattice structure of $KAlSi_2O_6$ (leucite), c) lattice structure of $NaAlSi_3O_8$ (albite).

As depicted in Fig. 6, the density of states in the valence band significantly exceeds that in the conduction band for both minerals, confirming that the conduction mechanism is primarily controlled by the hopping of K^+ and Na^+ ions. The activation energy (E_a) for both minerals can be determined using the equation $E_a = 0.5E_g$, where E_g represents the band gap in electron volts (eV). The calculated activation energy (E_a) for $KAlSi_2O_6$ and $NaAlSi_3O_8$ is 2.38 eV and 2.23 eV, respectively. These values are high and further confirm that the inherent ionic conductivity of the sea sand is low, resulting in a minimal contribution to the overall ionic conductivity of the C-SW-SS composite.
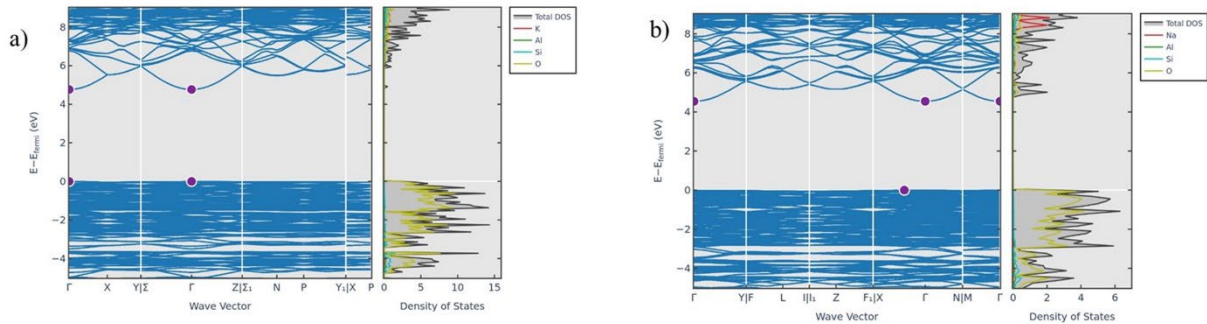
242

243 Figure 6. Energy band structure of the minerals. a) $KAlSi_2O_6$, b) $NaAlSi_3O_8$.

244 The elevated E_a values can be attributed to the lattice structure of $KAlSi_2O_6$ and $NaAlSi_3O_8$.

245 These minerals exhibit highly ordered crystalline structures comprising rigid $[AlSi_2O_6]$ and

246 $[AlSi_3O_8]$ units connected by strong and stable covalent bonds. Consequently, the lattices offer

247 limited interstitial sites for K^+ and Na^+ ions to occupy and provide few pathways for migration

248 between these sites due to the rigid Si-O and Al-O bonds [33]. In this case, the migration of

249 cations necessitates high thermal energy to 'hop' between interstitial sites.

250 *3.2.   Synergy between cement, seawater and sea sand during hydration*

251 Figure 7a shows a typical SEM image of the C-SW composite at 28 days. As depicted, the

252 microstructure of the C-SW composite is mainly composed of C-S-H with some ettringite and

253 calcium hydroxide $(Ca(OH)_2)$ phases. C-SW composites are known to exhibit more C-S-H

254 phases than normal cementitious materials [34-36]. This is due to the synergy effect between

255 OPC and the ionic species in seawater.
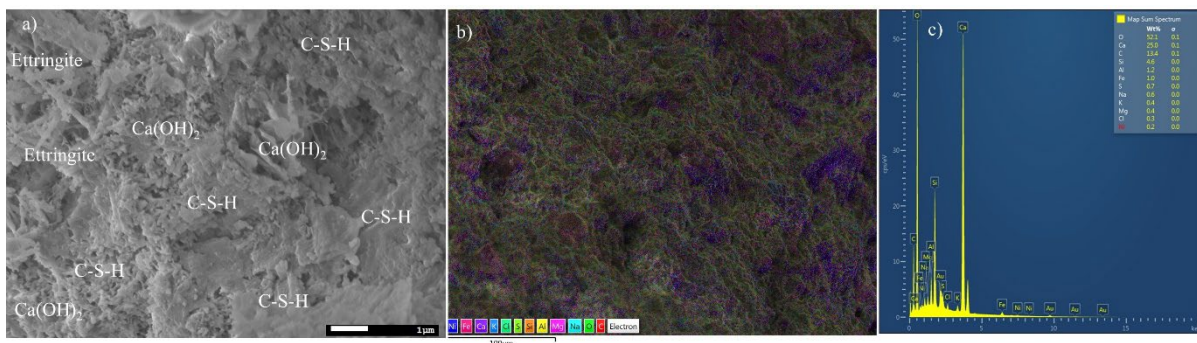
256

257 Figure 7. SEM and EDX elemental analysis of C-SW. a) SEM image, b) EDX layered SEM
258 image, c) EDX spectrum.

259　The high ion concentrations in the seawater tend to accelerate the early dissolution of the

260　calcium silicate phases in the cement by disrupting their interatomic bonding. This generates

261　additional Ca^{2+} and silicate species in the pore solution, enabling greater nucleation and growth

262　of C-S-H phases [37]. Among the various cationic species present in seawater Mg^{2+} ions

263　provide benefits for the C-S-H formation. The Mg^{2+} ions adsorb onto the surface of C-S-H

264　particles and interact with silicate, thus inhibiting crystallization and silicate polymerization of

265　C-S-H [38]. This generates disordered and porous C-S-H gel structures that can accommodate

266　high ion loading for ion exchange with the sea water. The high Cl^- ions participate in charge

267　balancing and develops the pore solution ionic strength needed for dissolution of the calcium-

268　silicate phases and precipitation of more C-S-H and other hydration products [39]. They also

269　promote substitution into C-S-H interlayers and absorption onto the particle surfaces to counter

270　cationic sites. The SO_4^{2-} anions are well known to allow the formation of ettringite in early

271　hydration which retains aluminum in the paste while releasing additional calcium for C-S-H

272　formation. Figure 7c depicts EDX elemental analysis of C-S-H in the C-SW composite. As

273　seen in this figure, the detected principle ionic species in the C-SW composite are Na^+, K^+,

274　Mg^{2+} and Cl^- at concentrations of 0.6, 0.4, 0.4 and 0.3%, respectively.

275

276　Figure 8. SEM and EDX elemental analysis of C-SW-SS. a) SEM image, b) EDX layered SEM
277　image, c) EDX spectrum.

278　As shown in Fig. 8a, the addition of sea sand increases the concentration of C-S-H phases. The

279　SiO_2 rich sea sand provides additional reactive silica that undergoes pozzolanic reactions with

280　$Ca(OH)_2$ formed during the hydration to generate supplementary C-S-H phases. The detected

281 principle ionic species in the C-SW-SS composite are also Na^+, K^+, Mg^{2+} and Cl^- at

282 concentrations of 0.7, 0.4, 0.6 and 1.2%, respectively.

283 As depicted in Figs. 9 and 10, the uniform distribution of Na^+, K^+, Cl^-, and Mg^{2+} ions revealed

284 by EDX elemental mapping in both composites implies that these ions are well-dispersed

285 within the C-S-H gel networks. The concentration of the detected ionic species is due to the

286 synergy between the sea water and C-S-H during hydration.
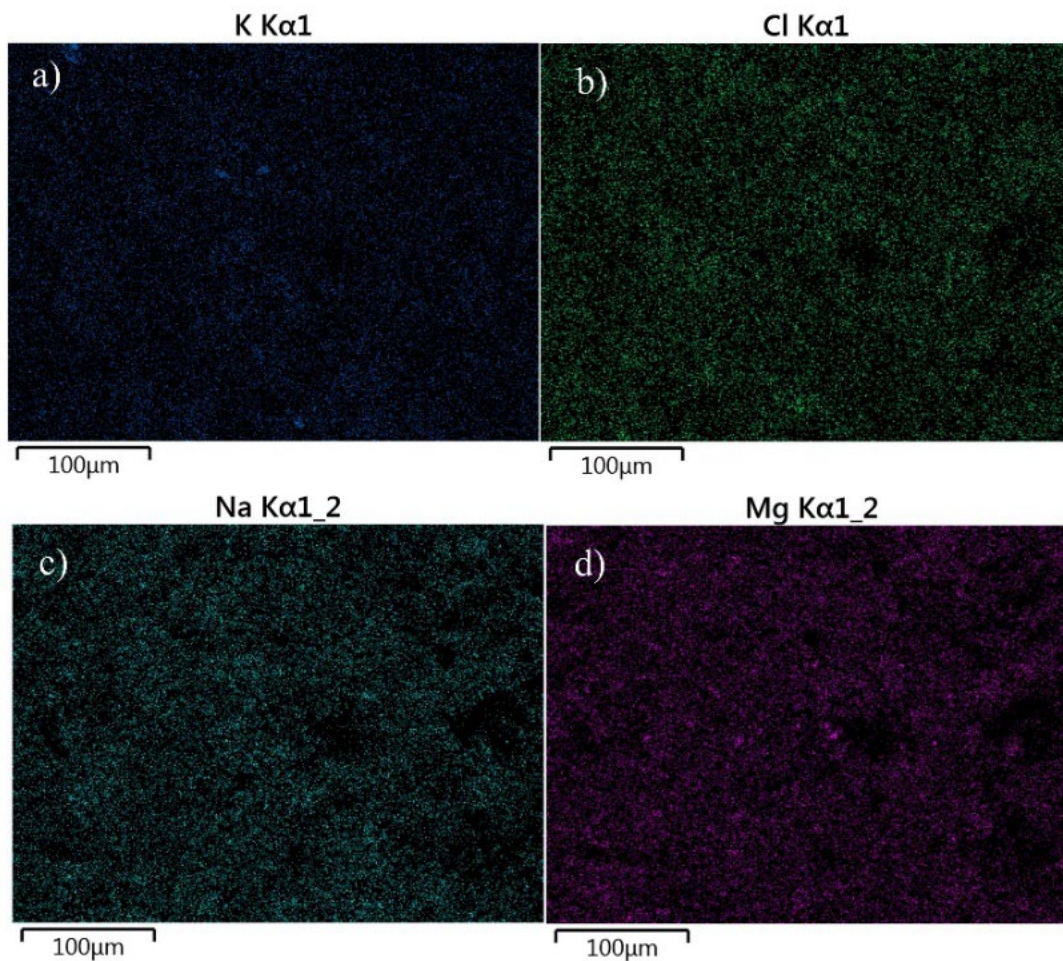
287

288 Figure 9. EDX element maps in C-SW. a) K element map, b) Cl element map, c) Na element
289 map, d) Mg element map.

290 C-S-H phases in cementitious materials typically possess an intrinsic ion exchange capacity

291 due to the presence of charged surface sites and interlayer spaces. The negatively charged

292 silicate groups on C-S-H surfaces enable exchange with cations, while anion exchange occurs

293 concurrently to balance charges. In this case, the Na^+ and K^+ cations from the sea water directly

294   exchange with Ca^{2+} in the C-S-H interlayer sites, whereas the Cl^- anions from the seawater

295   exchange with hydroxide (OH^-) groups in the C-S-H interlayers and those bound to silicate

296   groups at the structure surface and within chain sites to maintain charge neutrality. The divalent

297   Mg^{2+} cations do not readily exchange with Ca^{2+} in C-S-H due to charge and size mismatch. As

298   discussed above, the Mg^{2+} ions predominately play a role in stabilizing the C-S-H structure and

299   hindering its crystallization. This helps maintain high surface area for ion exchange sites.
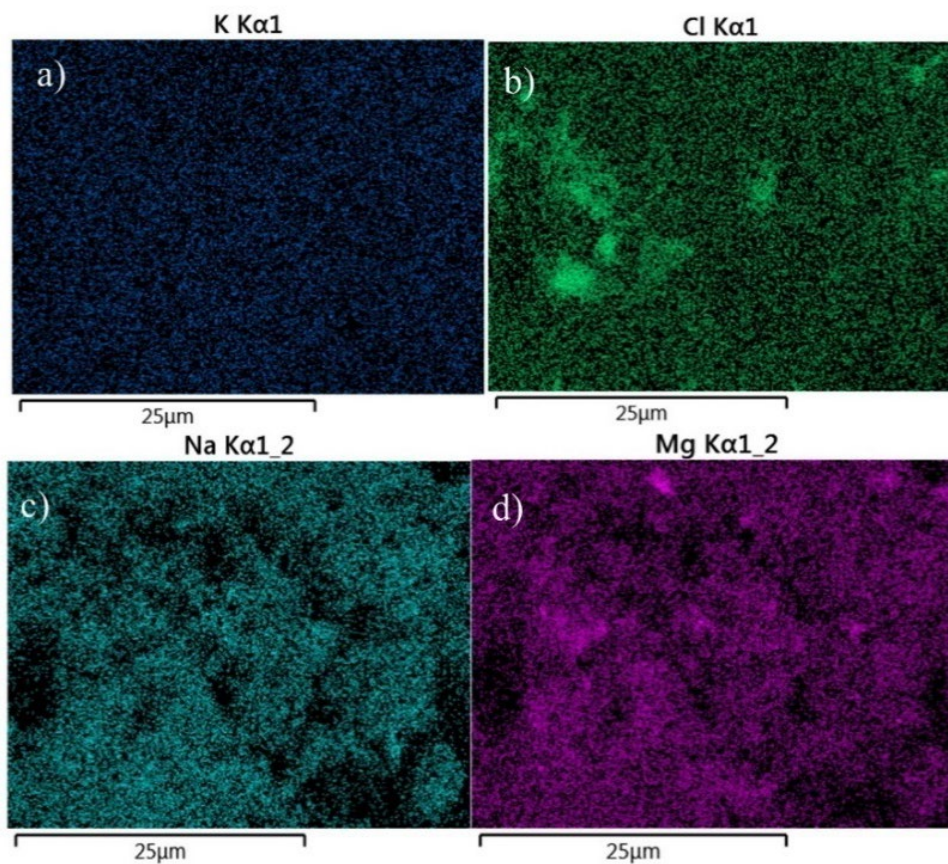
301   Figure 10. Element maps in C-SW-SS. a) K element map, b) Cl element map, c) Na element
302   map, d) Mg element map.

303   The addition of the sea sand into the C-SW-SS composite enhanced the ion exchange

304   mechanism, thereby increasing the concentration of Na^+, Mg^{2+} and Cl^-. We hypothesize that his

305   is due to the intrinsic porosity and surface roughness characteristics of the granular sea sand

306   particles that provide additional interfacial surface area between the aqueous seawater solution

307   and the C-S-H gel phases within the cement matrix. We believe that the rough surface and

308   intrinsic porosity of the sea sand expose more charged sites on the silica that can interact with

309   ions in the sea water solution. This provides increased cation and anion binding capacity. The

310   pores in the sea sand allow seawater to penetrate deeper and interact with more C-S-H surface

311   area that would otherwise be inaccessible, bringing more ions into contact with the C-S-H

312   phases. The sea sand porosity also allows localization of seawater ions near the C-S-H surfaces.

313   This creates a concentration gradient that drives the thermodynamically favorable ion exchange

314   at the interfaces. Thus, the enlarged seawater-C-S-H interfacial region created by the porous

315   sea sand enables more individual cation exchange and anion binding reactions to occur by

316   making more exchange sites available to more ions via enhanced accessibility and concentrator

317   gradients.

318   For the C-SW composite, the observed ion concentrations (Na^+, Mg^{2+} and Cl^-) are lower than

319   those in the C-SW-SS composite. This is due to the inefficiency of the direct ion exchange

320   between the seawater ions and the C-S-H phases. Although Na^+, Mg^{2+} and Cl^- ions are

321   abundantly present in the sea water, their efficient exchange with the inherent Ca^{2+} ions in the

322   C-S-H gels is restricted. We hypothesize that these mobile cations and anions first need to

323   diffuse through the pore solution before interacting with the C-S-H surfaces. This long-range

324   migration limits the population of monovalent and divalent ions that can be incorporated into

325   the C-S-H structure. Unlike Na^+, Mg^{2+}, and Cl^-, the K^+ concentrations remained equal between

326   the C-SW (0.4-wt%) and the C-SW-SS (0.4-wt%) composites. This is likely because the K^+

327   content in seawater itself is far lower compared to the other ions. Thus, the K^+ ion exchange

328   sites on the sea sand surface area become saturated faster as its overall lower concentration

329   restricts additional uptake. As such, the limited K^+ quantity in the seawater ions source curtails

330   extra incorporation, despite the enhanced ion exchange capacity enabled by the added sea sand.

331   3.3.   *Impedance response of C-SW and C-SW-SS composites*

332   The Bode plots of the real impedances for the composites are presented in Fig. 11. As

333   illustrated, the impedance response of the C-SW composite exhibits distinct characteristics

334   compared to the C-SW-SS. At 7 days, the impedance of the C-SW composite is controlled by

335   the relatively large and interconnected capillary pores and the nanoscale C-S-H morphology

336   within the bulk cement matrix. At lower frequencies, the impedance of the C-SW composite is

337   dominated by the large capillary pores whereas at higher frequencies, the impedance is

338   governed by the nanoscale C-S-H pores. At higher frequencies, the rapid alternating current

339   forces the ions to only flow through the shortest available C-S-H pores and channels. This

340   restricts the ion motion to small gel pores with short diffusion pathways which results in lower

341   real impedance. At lower frequencies, the ions have sufficient time to migrate through larger

342   pores and channels as the alternating current changes slowly. This allows access to more

343   tortuous pathways around the hydration products. The longer pathway length increases both

344   the ionic resistance and thus the real impedance.

345   At early age (7 days), the real impedance at low frequencies is initially low due to ion

346   conduction through the tortuous but interconnected capillary pores. As the curing progresses

347   (14 and 28 days), the large capillary pores get filled in by a dense C-S-H network composed of

348   segmented C-S-H gels. The segments within the C-S-H network act as diffusion barriers,

349   hindering the movement of ions between the segments which increases the ionic resistance of

350   the C-SW composite. This causes the real impedance at low frequencies to increase at later

351   curing ages as the C-S-H phases become dominant. At 14 and 28 days, the impedance response

352   of the C-SW composite at higher frequencies becomes similar to the impedance behavior at 7

353   days, where the small C-S-H gel pores controlled its response.
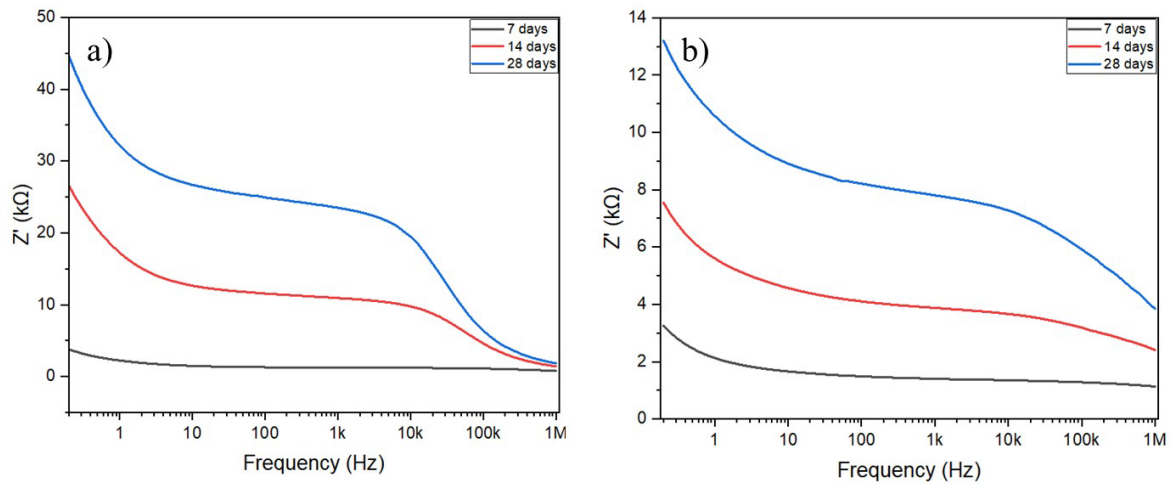
Figure 11. Bode plot of the real impedance. a) C-SW, b) C-SW-SS.

In contrast, the C-SW-SS composite displays significantly lower overall impedance values, reflecting a more ionically conductive system. The inclusion of the sea sand particles in the cement paste provides an interconnected network of pores. The size of these sea sand pores formed between the crystalline silicate grains are typically much larger compared to the nanometer-scale C-S-H gel pores. This significant difference in pore size and continuity results in substantially increased ion mobility through the sea sand pore network compared to the highly disconnected C-S-H gel pores in the C-SW composite.

Figure 12 depicts the Bode plots of the imaginary impedances. As shown in Fig. 12a, the C-SW displays high imaginary impedance values at low frequencies owing to significant resistive losses associated with the electrical double layer polarization at the pore-ion interface. The alternating current field at low frequencies allows sufficient time for migration and accumulation of ions and dipolar water molecules from the bulk pore solution onto the negatively charged C-S-H gel pore surfaces. The alignment and stacking of these adsorbed ions and oriented water dipoles forms a stern layer at the interface thereby hindering ionic mobility.
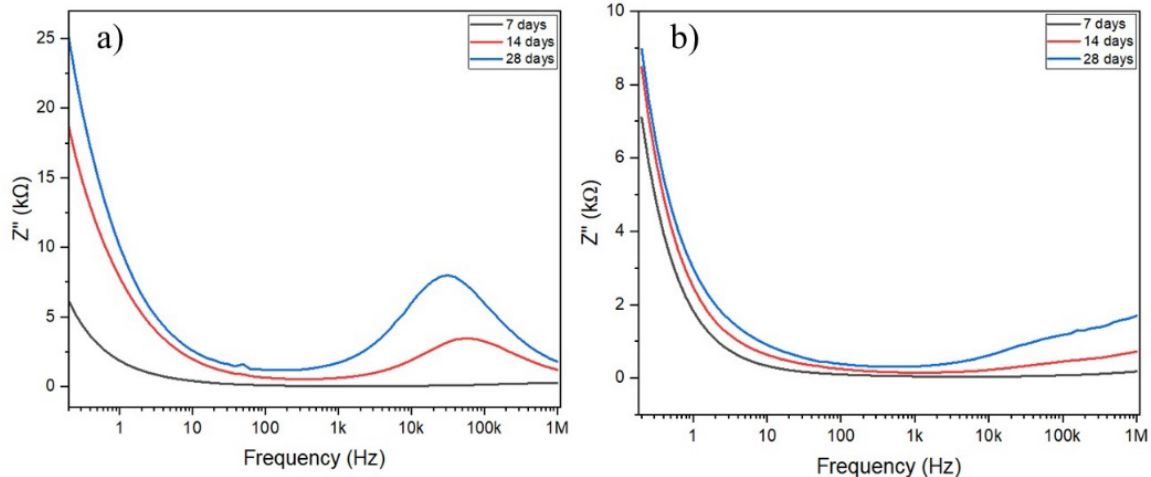
Figure 12. Bode plots of the imaginary impedances. a) C-SW, b) C-SW-SS.

The energy dissipated in establishing this polarized layer through charge separation manifests as resistive losses which increases the imaginary impedance components. As the frequency increases, the rapid alternation of the applied electric field provides inadequate time for the sustained ion migration and water dipole reorientation needed to maintain the polarized stern layer. Therefore, the magnitude of interfacial polarization and associated with the resistive losses decreases significantly with increasing frequency above 10 Hz, as evidenced by the rapid reduction in the imaginary impedance. Additionally, at higher frequencies the alternating current is constrained to surface regions and smaller intrinsic gel pores rather than penetrating deeper into the microstructure. This reduces its interactions with the pore fluid, further decreasing the resistive losses. The peaks in the imaginary impedances observed at intermediate frequencies around 10-40 kHz after 14 and 28 days of curing may suggest dielectric relaxation processes involving the redistribution of ions incorporated into the C-S-H nanostructure in response to the alternating field. The increasing imaginary impedance at lower frequencies with curing age is due to the progressive restrictions in ionic migration pathways as hydration proceeds. The formation of disconnected C-S-H nanopores over time hinders ion motion under the slowly alternating current. This causes growing phase lags as ions are not able to keep pace with the changing AC signal due to transport limitations in the segmented C-S-H network. This leads to larger imaginary impedance values.

390   The C-SW-SS composite, however, exhibits remarkably lower imaginary impedance values

391   over the entire frequency spectrum owing to the abundant ions in C-S-H and interconnected

392   sea sand pores (Fig. 12b). The high ionic content and continuity of pores allows charge carriers

393   to migrate with ease, thereby lowering the impedance values compared to the C-SW-SS

394   composite. Importantly, the imaginary impedance response of the C-SW-SS composite remains

395   low even after 28 days of air curing, with negligible changes compared to 7 days. This indicates

396   the C-SW-SS composite maintained its interconnected pores which preserve ion mobility

397   pathways. This can allow the composite material to hold electrical charges which can function

398   as a solid-state electrolyte for large-scale electrochemical energy storage applications in

399   supercapacitors and batteries.

400   *3.4.   Phase response of C-SW and C-SW-SS composites*

401   The Bode plots of the phase angles of the cementitious composites are shown in Fig. 13. The

402   phase angle represents the relative contribution of the resistive and capacitive components

403   controlling the overall impedance of the cementitious composites. As depicted in Fig. 13a, for

404   the C-SW composite, at low frequencies, the high negative phase angles indicate the response

405   is dominated by the resistive losses through the bulk cementitious composite and the

406   interconnected capillary pores. As the frequency increases, the decreasing phase angle suggests

407   a transition to more capacitive effects, presumably from the electrical double layer formation

408   at the pore surfaces. The peak phase angle of -5 degrees at 300 Hz at 7, 14 and 28 days suggests

409   a resonance point where the resistive and capacitive impedance components equalize. Beyond

410   the peak frequency, the reduction in the phase angles indicates a transition to capacitive effects

411   becoming more influential than the resistive losses in controlling the impedance. This

412   capacitive response arises from the formation of electrical double layers by migration and

413   accumulation of ions and oriented water dipoles at the pore-fluid interface. The slope of the

414   phase angle decreases with frequency at later curing ages implies that as the curing age

415 increases, the continued hydration refines pores, increasing capacitive effects compared to the

416 initial resistive pore network. As can be seen in Fig. 13b, the C-SS-SW composite displays a

417 peak phase angle at a higher frequency around 1 kHz owing to the pervasive conductive sea

418 sand pore network which dominates the resistive response over a wider frequency band. The

419 interconnected sea sand pores facilitate substantial ion motion, necessitating higher frequencies

420 for capacitive effects to become prominent.
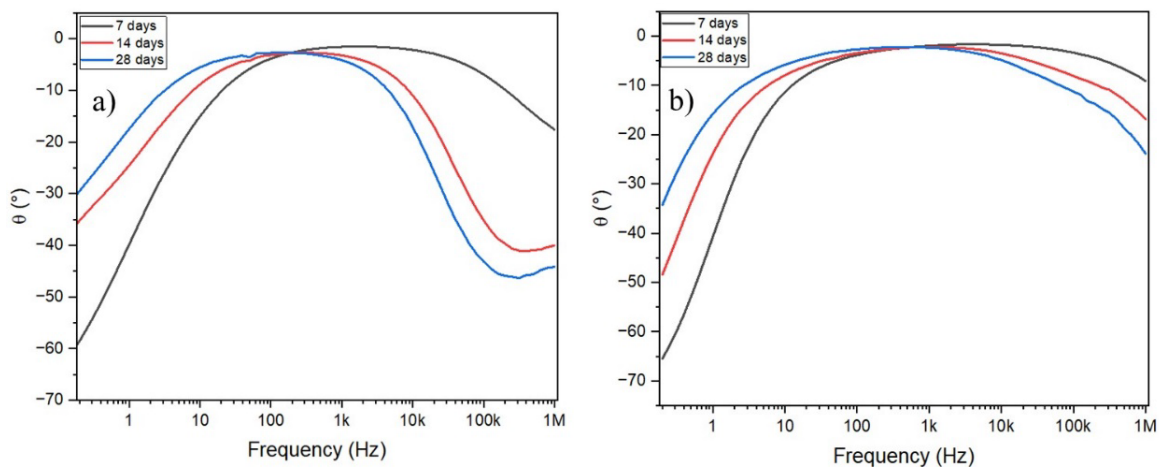
421

422 Figure 13. Bode plots of phase angle. a) C-SW, b) C-SW-SS.

423 The frequency at which the phase angle reaches a maximum indicates the relaxation time

424 constant of the system. This relaxation time represents the time taken for ions to diffuse and

425 redistribute in response to the alternating field and can be calculated using the following

426 equation:

427
$$t = \frac{l^2}{2D} \qquad (1)$$

428 where l is the diffusion distance for the ionic species and D is the diffusion coefficient of the

429 ionic species. The C-SW composite shows a peak phase angle at around 300 Hz for all curing

430 ages. This implies an ionic diffusion time constant on the order of milliseconds. For the C-SW-

431 SS composite, the peak occurs at a higher frequency of ~1 kHz for all curing ages. This suggests

432 a faster ionic diffusion time in the microseconds range. The ubiquitous conductive sea sand

433 pores allow easier ion motion, thereby reducing the diffusion time constant compared to the C-

434 SW composite.

435 *3.5.   Electrochemical behavior of C-SW and C-SW-SS composites*

436 As shown in Fig. 14, the Nyquist response of the C-SW composite displays characteristically

437 semicircles in the high frequency region, indicating substantial polarization resistance to ionic

438 flow through its microstructure. This stems from the discontinuous nature of the intrinsic C-S-

439 H gel nanopores which severely impedes ion mobility and increases impedance. Although the

440 diameter of the semicircle increases with curing age as more nanostructured C-S-H forms, the

441 fundamental morphology restricts ion diffusion. This increases the semicircle size, reflecting

442 greater polarization resistance as hydration progresses.

443 The pronounced low frequency Warburg-type tail signifies diffusion-limited ion transfer likely

444 through the larger capillary pores between the unhydrated cement grains. As the hydration

445 proceeds, this tail grows due to increased diffusion length scales caused by accumulation of

446 nanostructured C-S-H on the pore surfaces. The evolution from initially facile diffusion

447 through interconnected capillary pores to obstructed conduction highlights the C-SW

448 composite's poor ionic diffusivity.
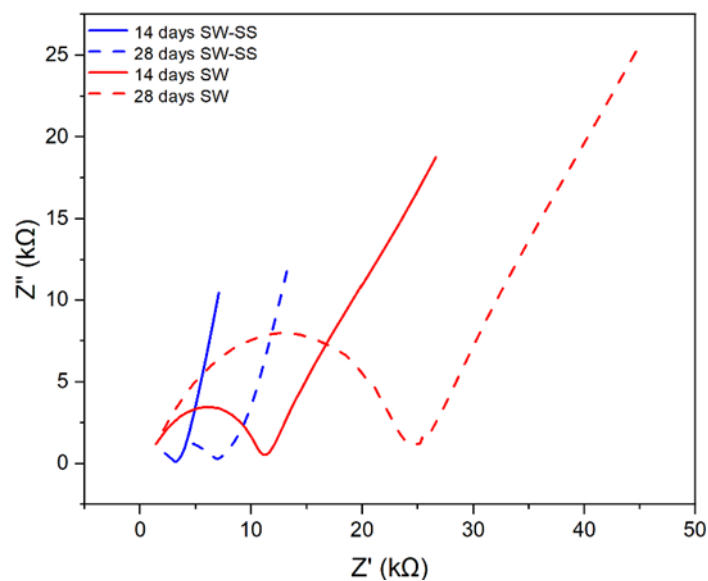
449
450   Figure 14. Nyquist plots for C-SW and C-SW-SS composites at 14 and 28 days.

451   The C-SW-SS composite, however, exhibits remarkably different Nyquist plots owing to its

452   higher ion concentrations and ubiquitous interconnected sea sand pores transporting the ionic

453   species. The micrometer-sized sea sand pores allow ion motion with minimal impediments,

454   significantly reducing polarization resistance compared to the C-SW composite. As a result,

455   the C-SW-SS composite displays a pronounced Hook response in the high frequency region

456   which attributed to capacitive effects from the pervasive ionic movement through its

457   conductive pore network. The lack of a low frequency resistive tail indicates substantially

458   higher ionic diffusivity compared to the C-SW composite. The ease of ion migration through

459   the interconnected sea sand pores is evidenced by the dominating Hook response that persists

460   through all curing ages.

461   The diffusion coefficient D of the ionic species in Eq. (1) can be described by the following

462   equation [40]:

463
$$D = \frac{R^2 T^2}{2n^4 F^4 A^2 C^2 \sigma^2} \tag{2}$$

464   where R is the gas constant, T is the absolute temperature, n is the number of the electrons per

465   molecule involved in the charge transfer process, F is the Faraday constant; A is the surface

466   area of the electrodes; C is the concentration of the ionic species in the cementitious composite

467   and σ is the Warburg diffusion coefficient. As shown in Eq. (2), the diffusion coefficient D is

468   controlled by the Warburg diffusion coefficient σ. When σ increases, the diffusion process in

469   the composite becomes slower, and when σ decreases, the diffusion process in the composite

470   becomes faster. In the low frequency region, the relationship between the Warburg diffusion

471   coefficient σ, the charge transfer f_{ct} and the real impedance Z' is given by the following equation

472   [41]:

473
$$Z' = f_{ct} + \sigma \omega^{-1/2} \tag{3}$$

474   where ω is the angular frequency. Figure 15 plots the real impedance Z' versus the inverse

475   square root of the angular frequency ($\omega^{-1/2}$) and the slopes of the fitted linear lines are the

476   Warburg diffusion coefficients σ which are given in the figure. The effect of curing age on the

477   Warburg diffusion coefficient σ is shown in Fig. 16.
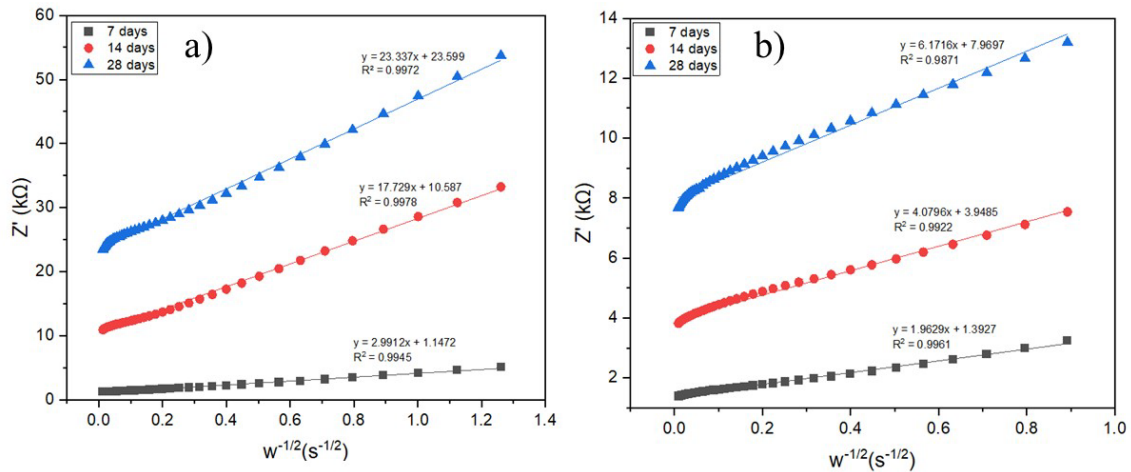
478

479   Figure 15. Warburg diffusion coefficient vs $\omega^{-1/2}$. a) C-SW, b) C-SW-SS.

480   As shown in Fig. 16, the Warburg diffusion coefficient σ increased with curing age. This means

481   the diffusion of the ionic species slows down as the curing process progresses due to loss of

482   moisture. However, the C-SW-SS composite exhibited much lower Warburg diffusion

483   coefficients σ than the C-SW composite. The values at which the fitted linear lines cross the

484   impedance axis (i.e., Z') represent the charge transfer resistance R_{ct}. The variation of R_{ct} as a

485   function of curing age is given in Fig. 17. The figure indicates that R_{ct} of the composites

486   exhibits an increasing trend with curing age similar to that of the Warburg diffusion coefficient

487   σ. Figure 17 also shows that the R_{ct} values of the C-SW-SS composite are much lower than

488   those of the C-SW composite. This again confirms that the sea sand promotes diffusion of ions

489   which in turn reduces R_{ct}.

490

491

492

493
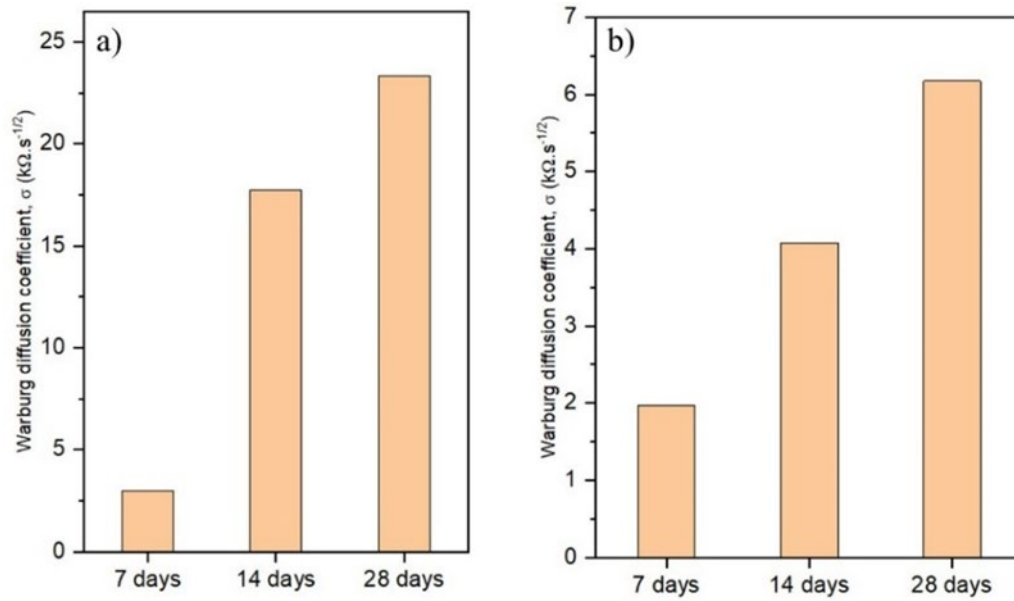
Figure 16. Effect of curing age on Warburg diffusion coefficient σ. a) C-SW, b) C-SW-SS.

495
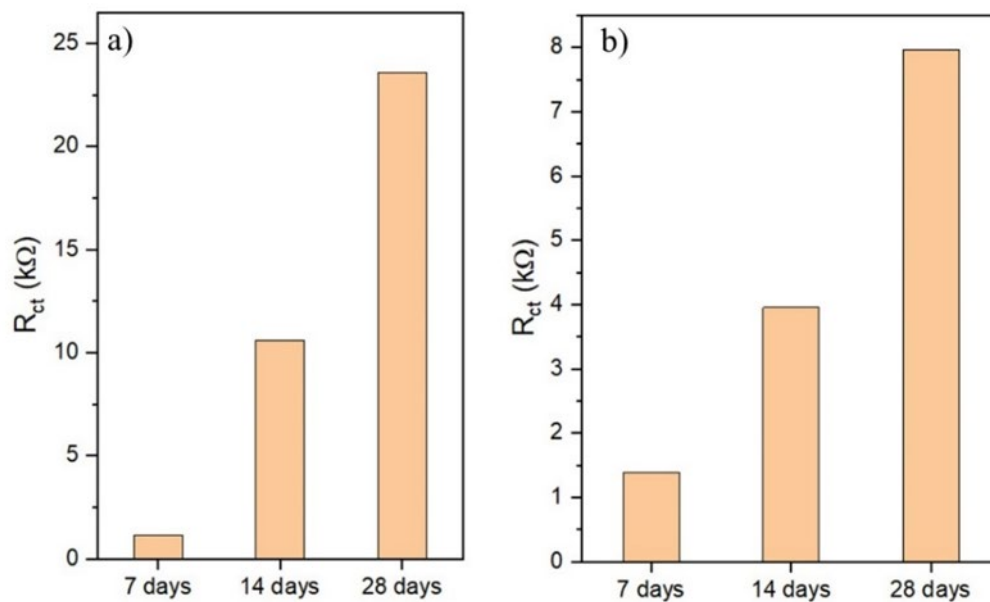
Figure 17. Effect of curing on the charge transfer resistance. a) C-SW, b) C-SW-SS.

3.6. Analysis of ion accumulation in C-S-H and the influence of anions and cations on electrical properties

The incorporation of exchanging ions into the C-S-H gel pores provides a reservoir of mobile ions along with native Ca^{2+} ions (Fig. 18b). These species migrate and accumulate at the negatively charged C-S-H surfaces under an applied field. As shown in Fig. 18c, the combined accumulation of both native and exchanged ions enables the development of an electrical

503 double layer (EDL) structure within the intrinsic C-S-H pores where the rigidly bound ions are

504 in the compact layer (Stern layer) and the mobile ions are in the diffuse layer. In this case, the

505 exchanged Na^+ and K^+ cations and especially the native divalent Ca^{2+} are accumulated in the

506 compact/stern layer of the C-S-H electrical double layer (EDL), while the exchanged Cl^- anions

507 are distributed in the diffuse layer. This creates a high concentration of positive charge at the

508 C-S-H surface and an associated strong positive electric potential.
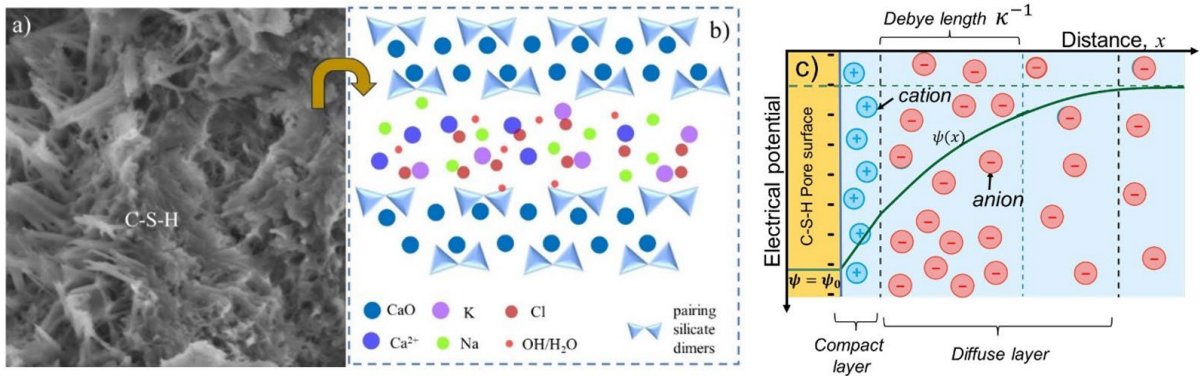
510 Figure 18. a) typical SEM image of C-S-H gel in C-SW-SS, b) sketch of typical C-S-H
511 molecule structure acting like ionic sponge, c) C-S-H with ions treated as an electrical double
512 layer.

513 As shown in Fig. 18c, the separation of charge between the cation and negative C-S-H pore

514 surface sets up an electric field $E(x)$ that causes the potential $\psi(x)$ to decay with distance from

515 the surface according to the following equation [42]:

$$\psi(x) = \psi_0 \, exp\left[\frac{-xe^2}{\varepsilon k_B T}\sum \eta_\pm q_\pm\right] \tag{4}$$

517 where $\psi(x)$ is the electrical potential at a distance x from the charged C-S-H pore surface, ψ_0

518 is the potential at the C-S-H pore surface, $(x = 0)$, η_+ is the concentration of cations (Na^+, K^+

519 and Ca^{2+}), η_- is the concentration of anions (Cl^-), q_+ is the cation charge number, q_- is the

520 anion charge number, e is the electron charge, ε is the permittivity, k_B is the Boltzmann

521 constant and T is the temperature.

522 The EDL electrical field $E(x)$ decay is given by the following equation:

$$E(x) = \frac{d\psi(x)}{dx} = \psi_0 \left(\frac{e^2}{\varepsilon k_B T}\right)\left(\sum \eta_\pm q_\pm\right) exp\left[\frac{-xe^2}{\varepsilon k_B T}\sum \eta_\pm q_\pm\right] \tag{5}$$

524   The electrical potential ψ_0 ($at\ x = 0$) and the electrical field E_0 ($at\ x = 0$) at the C-S-H

525   surface are given by the following equations:

526
$$\psi_0 = \left(\frac{2RT}{F}\right) sinh^{-1}\left(\frac{\sigma}{F \sum e\eta_\pm\ q_\pm}\right) \tag{6}$$

527
$$E_0 = \psi_0\left(\frac{e^2}{\varepsilon k_B T}\right)\left(\sum \eta_\pm\ q_\pm\right) \tag{7}$$

528   Where F is the Faraday's constant, R is the ideal gas constant and σ is the surface charge density.

529   From the above equations we can see that the formation of ψ_0 and E_0 in the C-S-H EDL is

530   driven primarily by the accumulation of cations near the negatively charged C-S-H surface.

531   The cations Na^+, K^+, and especially the divalent Ca^{2+}, are electrostatically attracted to the stern

532   layer. This creates a high concentration of positive charge at the C-S-H surface which in return

533   produces strong surface potential ψ_0 and electrical field E_0. The Cl⁻ anions in the pore solution

534   diffuse layer balance the cation accumulation and form the negatively charged diffuse layer.

535   The Cl⁻ anions have a smaller effect on the potential due to their -1 charge. The higher +2

536   charge of Ca^{2+} ions results in a greater buildup of positive surface charge density (σ) compared

537   to Na^+ and K^+. The Ca^{2+} ions thus make the strongest contribution to the formation of ψ_0 and

538   E_0 near the C-S-H surface. In this case, the combined effects of Ca^{2+}, Na^+ and K^+ dominate and

539   lead to large ψ_0 and E_0 values which overcome the reducing effects of Cl⁻ ions.

540   The charge separation at the C-S-H surface creates a substantial electric field E_0 promoting

541   efficient electromigration of ions through the interconnected pores. The ionic conductivity of

542   the cementitious composites under the surface electrical field due to the accumulation of

543   cations is described by the following equation [32]:

544
$$\sigma_{ion} = \sigma_0 exp\left(\frac{eq_+ E_0}{K_B T}\right) \tag{8}$$

545   where σ_0 is the ionic conductivity without electric field (just diffusion). Equation (8) indicates

546   that the ionic conductivity of the cementitious composites is strongly dependent on the

547 concentration of cations and the surface electrical field (E_0). The higher the cation

548 concentration in the compact EDL and E_0, the higher the ionic conductivity. The enhanced ion

549 exchange capacity in C-SW-SS promotes greater accumulation of cations on the C-S-H pore

550 surfaces. The higher cation concentration generates a stronger sustained electric field E_0. This

551 higher field provides the force necessary to maintain continuous ion motion within the confined

552 C-S-H layers. The increased field-driven ion transport enabled by the cation accumulation

553 resulting from the superior ion exchange kinetics directly improves the overall ionic

554 conductivity of the C-SW-SS composite compared to the C-SW composite.

555 *3.7.   Summary of conduction mechanisms in C-SW-SS and C-SW composites*

556 During the hydration process of the C-SW-SS composite, the first major conduction

557 mechanism is ion exchange between the seawater ions and the C-S-H gel phases. In the fully

558 hydrated state, the C-S-H gel phases have undergone extensive ion exchange with the seawater

559 ions, facilitated by the porous sea sand network. This results in a high concentration of mobile

560 charge carriers such Na^+, K^+, Mg^{2+}, Cl^-, and native Ca^{2+} incorporated within the C-S-H

561 structure. With the C-S-H gel network saturated with these mobile ions after the ion exchange

562 process, the primary conduction mechanism transitions from ion exchange to ionic diffusion

563 and migration within the C-S-H phases. This second mechanism, governed by diffusion and

564 migration processes, becomes the dominant pathway for ionic conduction in the fully hydrated

565 state.

566 The ionic diffusion process involves the random movement of incorporated ions driven by

567 concentration gradients within the C-S-H gel network. The ions effectively "hop" between

568 available sites within the disordered and less densified C-S-H structure facilitated by the sea

569 sand particles. Concurrently, the migration mechanism relies on the movement of ions due to

570 electric potential gradients. The charged ions experience electrostatic forces, driving their

571 movement through the C-S-H gel network and contributing to overall ionic conductivity. This

migration process also involves a "hopping" mechanism, where ions hop between charged sites within the C-S-H structure, influenced by the electric field.

The porosity, tortuosity, and microstructural characteristics of the C-S-H gel, significantly influenced by the sea sand particles, are crucial factors determining the efficiency of ionic conduction via diffusion and migration mechanisms. The interconnected pore structure created by the sea sand particles provides low-resistance pathways for the diffusion and migration of incorporated ions within the C-S-H gel network, enhancing overall ionic conductivity. These pathways facilitate efficient ion transport by reducing energy barriers and increasing the mobility of charge carriers through enhanced diffusion, hopping processes, and electric field-driven migration. Furthermore, the rough surfaces and intrinsic porosity of the sea sand particles contribute to a more disordered, less densified, and higher surface area C-S-H microstructure in the C-SW-SS composite. This disordered microstructure, with lower tortuosity, further facilitates efficient ionic mobility by reducing energy barriers for ion diffusion and migration, optimizing the ionic conduction pathways involving hopping processes and electric field-driven migration.

In contrast, despite the presence of mobile ions within the C-SW C-S-H gel phases from the initial ion exchange with seawater, the lack of an interconnected porous network and the higher tortuosity of the C-S-H microstructure impede efficient ion transport via diffusion and migration mechanisms in the fully hydrated state. The absence of sea sand particles in the C-SW system results in a denser and more closely packed C-S-H gel structure, increasing energy barriers for ion diffusion and migration processes. The limited porosity and higher tortuosity restrict the movement of ions, hindering their ability to "hop" between available sites within the C-S-H network and limiting pathways for electric field-driven migration, diminishing the efficiency of these conduction mechanisms.

3.8. Ionic resistivity of C-SW and C-SW-SS composites

597 The ionic conductivity σ_{ion} of the cementitious composites is intrinsically linked to their ionic

598 resistivity ρ_{ion} through the relationship $\sigma_{ion} = \dfrac{1}{\rho_{ion}}$. Enhancing the ionic conductivity therefore

599 requires reducing the ionic resistivity by facilitating ion transport through the cementitious

600 composites.

601 The ionic resistivity of the C-SW and C-SW-SS composites was calculated using the equation

602 $\rho_{ion} = R_{ion}\dfrac{A}{L}$ where A is the electrode contact area, L is the distance between the two

603 electrodes and R_{ion} is the ionic resistance. The ionic resistance of the cementitious composites

604 was calculated according to the methodology described in the experimental section. Figure 19

605 shows the effect of air curing age on the ionic resistivity of the cementitious composites. As

606 shown, the effect of curing on the ionic resistivity is similar to that on R_{ct}. At 28 days, the room

607 ionic resistivity of the C-SW-SS composite is about 25 kΩ.cm. This is about six times lower

608 than the ionic resistivity of the C-SW composite, which is around 165 kΩ.cm. The improved

609 ionic conductivity of the C-SW-SS composite places it in the range of solid-state electrolytes

610 currently used in energy storage technologies, which typically exhibit room temperature ionic

611 resistivities between 6 MΩ.cm and 0.3 kΩ.cm [43].

612 The 28-day resistivity of C-SW and C-SW-SS composites was compared with that of

613 conventionally moist-cured cementitious composites, both plain and conductively doped,

614 prepared with distilled water as per literature findings. As shown in Fig. 20, the comparison

615 shows that, in general, despite air curing, the C-SW-SS composite outperformed the moist-

616 cured ordinary cementitious composites with and without conductive additives in terms of

617 lower ionic resistivity. Additionally, the C-SW composites exhibited lower ionic resistivity

618 compared to the moist-cured plain ordinary cementitious composites.

619

620
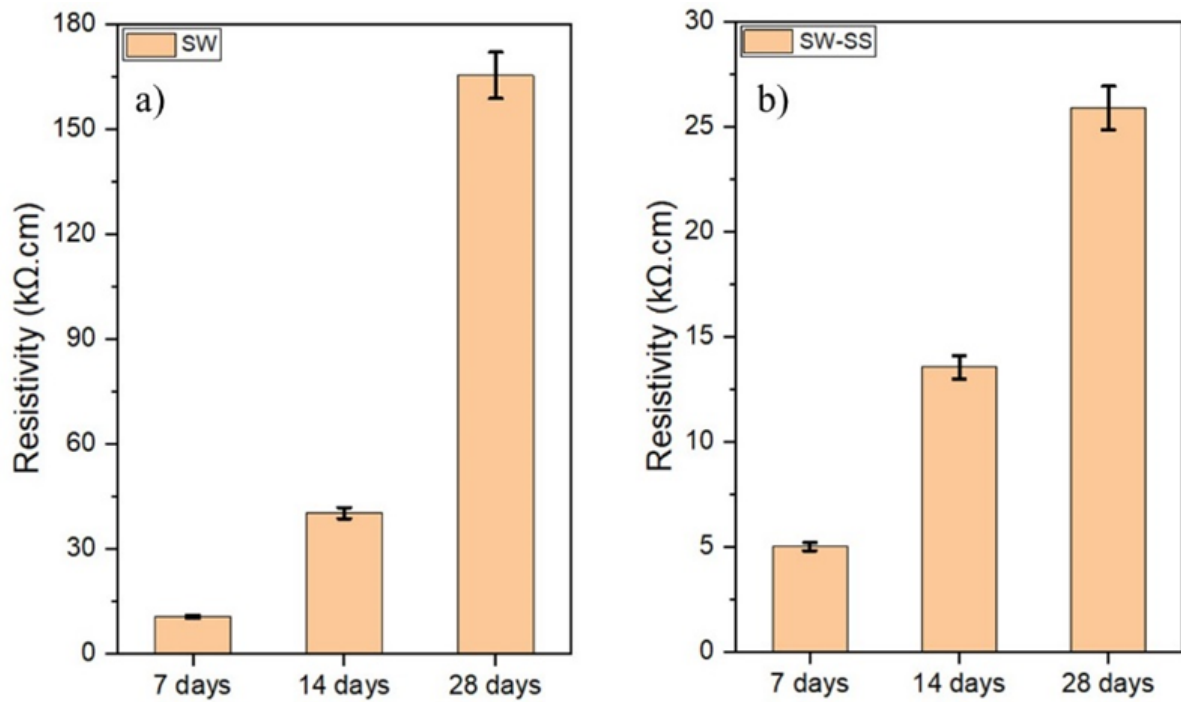
Figure 19. Effect of curing on the ionic resistivity. a) C-SW, b) C-SW-SS.

The superior performance of the C-SW-SS composites compared to plain conventional cementitious composites is attributed to the synergistic effects of sea water and porous sea sand, facilitating ion transport and exchange mechanisms within the composite matrix. In conventional cement composites with conductive fillers, the ionic conduction occurs primarily through the cement pore solution and relies on the formation of conductive pathways through the random dispersion of filler particles. However, the inherent tortuosity and discontinuity of these pathways, as well as the presence of resistive gaps between the filler particles, impede efficient ionic transport, leading to higher overall ionic resistivity.
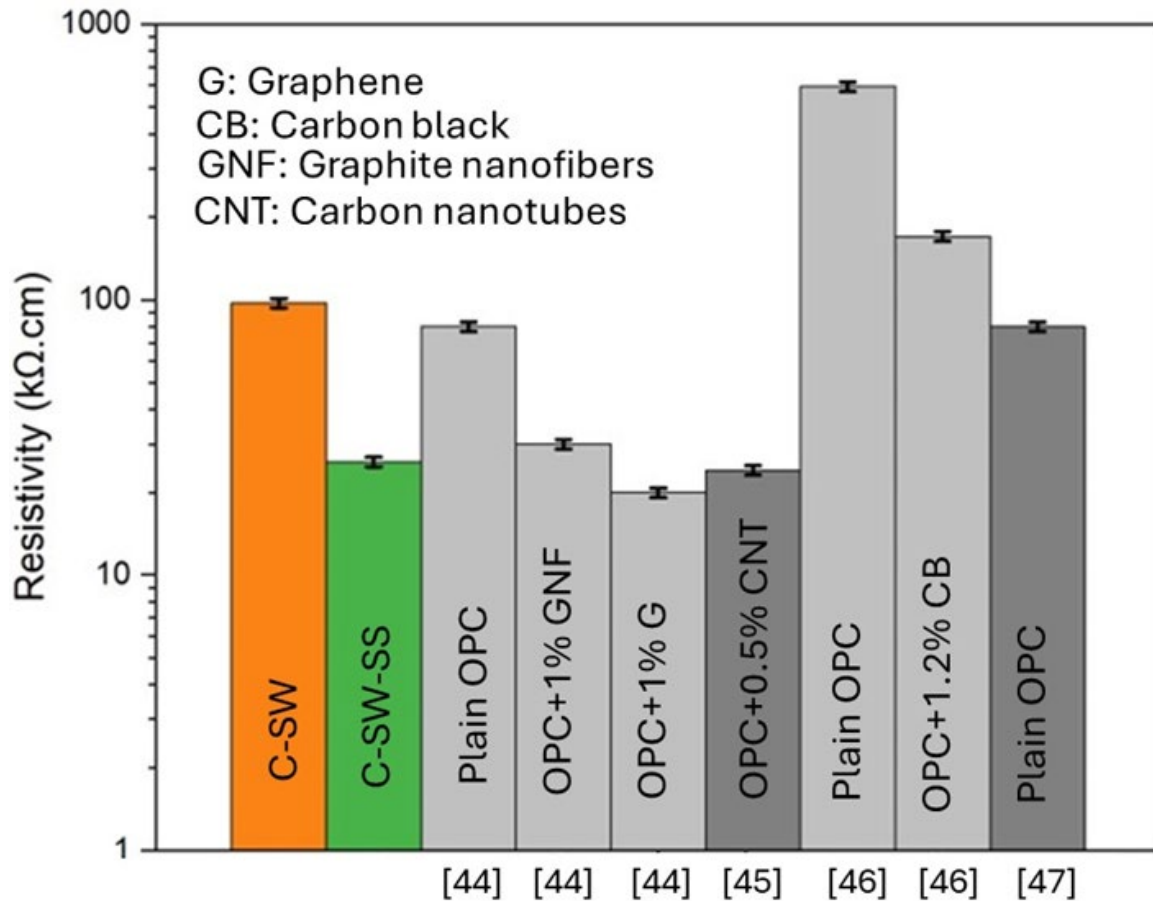
Figure 20: Comparison of ionic resistivity among C-SW, C-SW-SS, and conventional cementitious composites.

3.9.   Multifunctional capabilities of the C-SW-SS composite

Figure 21a shows the effect of the applied compressive load on the change in the bode plot of the real impedance of the C-SW-SS composite. The applied compressive load was converted to compressive stress and plotted against the change in the real impedance at a frequency of 2 kHz as depicted in Fig. 21b. From this figure, we can see that the change in the real impedance decreased significantly when the applied compressive stress is increased from 0 to 4 MPa. This decrease then slowed down and became constant at stresses higher than 4 MPa.

In the unstressed state, the ion conduction occurs via the inherent nanometer-scale pores-like channels within the C-SW-SS composite. The compressive stress reduces the hopping distance for ionic transport between the existing pores in composite. In this case, the pores are deformed which brings the pore networks in closer proximity, thereby shortening the distances between

645 pores. This lowers the activation energy for the conductive ion transport which reduces the real

646 impedance. This results in decrease in the measured real impedance between 0 to 4 MPa

647 compression. At higher compressive stresses, the change in the real impedance somewhat

648 becomes constant. This is because the change in the overall porosity and tortuosity stabilizes,

649 resulting in a consistent ion diffusion mechanism and no further change in the impedance. In

650 this state, the combination of intrinsic pores facilitates efficient ion transport under compressive

651 loading, resulting in a constant real impedance.

652 Figure 21b indicates that the stress sensitivity factor (i.e., stress gauge factor), K_Z decreases

653 with increasing compressive stress. This means the C-SW-SS composite is sensitive to low

654 levels of mechanical stress. This high responsiveness contrasts with traditional conductive

655 cement-based sensors which require larger strains before measurable signals. As such, the C-

656 SW-SS composite demonstrates promising capacity for continuous structural health

657 monitoring of concrete elements. Typical service stresses remain below material limits but can

658 accumulate damage over time. The C-SW-SS's exceptional sensitivity in the low mechanical

659 stress level enables detection of emerging deterioration thereby avoiding catastrophic failure

660 through early intervention.
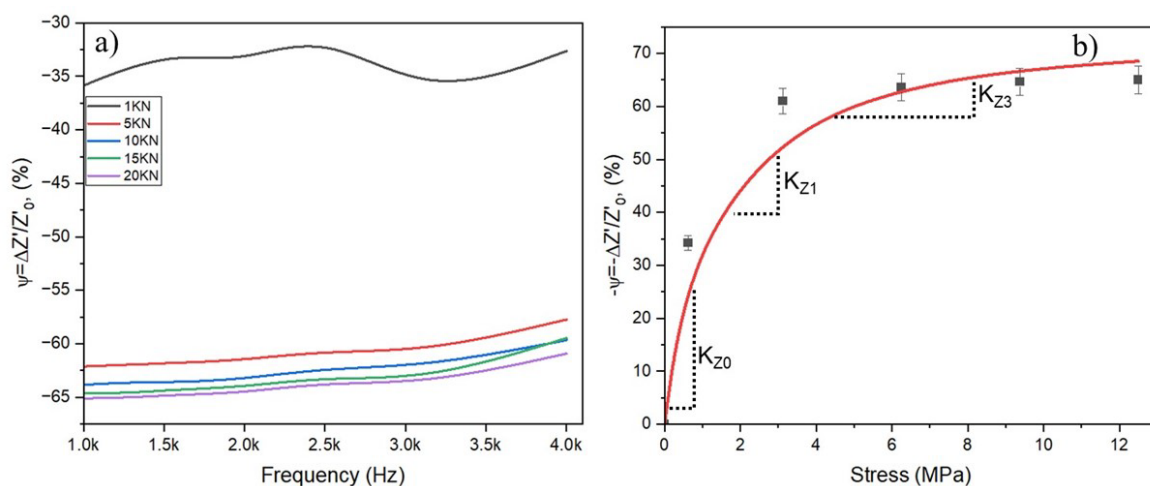
661

662 Figure 21. Response of the C-SW-SS to compressive stress. a) effect of compressive load on
663 the Bode plot of the change in the real impedance, b) compressive stress vs change in the real
664 impedance.

665   Figure 22 illustrates typical CV curves for the C-SW-SS composite at both 7 and 28 days air

666   curing using various scan rates. It is important to note that at lower scan rates and after 28 days,

667   unexpected noise in the CV curves was captured by the Gamry EIS system. However, this noise

668   has no discernible effect on the overall cyclic voltammetry response of the cementitious

669   composites. At the scan rate of 50 mV/s (Fig. 21a), the CV curve has a parallelogram like-

670   shape between -1 V and + 1V, indicating EDL capacitance as the primary charge storage

671   mechanism. The cations and anions within the C-SW-SS composite migrate and accumulate at

672   the polarized electrodes to balance surface charges in the EDL. As the scan rate increases to

673   100 mV/s and beyond, the CV curves become angled leaf-like shapes as diffusion outpaces

674   reactions. The main cations-based charge carriers in the EDL include Ca^{2+}, Na^+ and K^+. These

675   cations are concentrated in the compact Stern layer on the negatively charged C-S-H phases,

676   paired with mobile Cl^- anions diffusing in the porous channels. The sea sand particles provide

677   interconnected void spaces enabling ion penetration into the cement bulk. As such, when the

678   voltage increases, more EDL layers form which result in higher capacitive current response,

679   forming angled leaf-like CV shapes.

680   As illustrated in Fig. 22, the CV signature shapes remain somewhat unchanged even after 28

681   days of air curing when compared to the results observed after 7 days, demonstrating the

682   electrochemical charge retention capacity of the C-SW-SS composite. The maintained CV

683   shapes over repeated voltage cycling, even in low moisture conditions, confirms durable and

684   reversible ion storage properties. The electrochemical charge retention ability of the C-SW-SS

685   composite shows its potential as a novel solid state electrolyte material for cement-based

686   electrical energy storage in concrete structures.
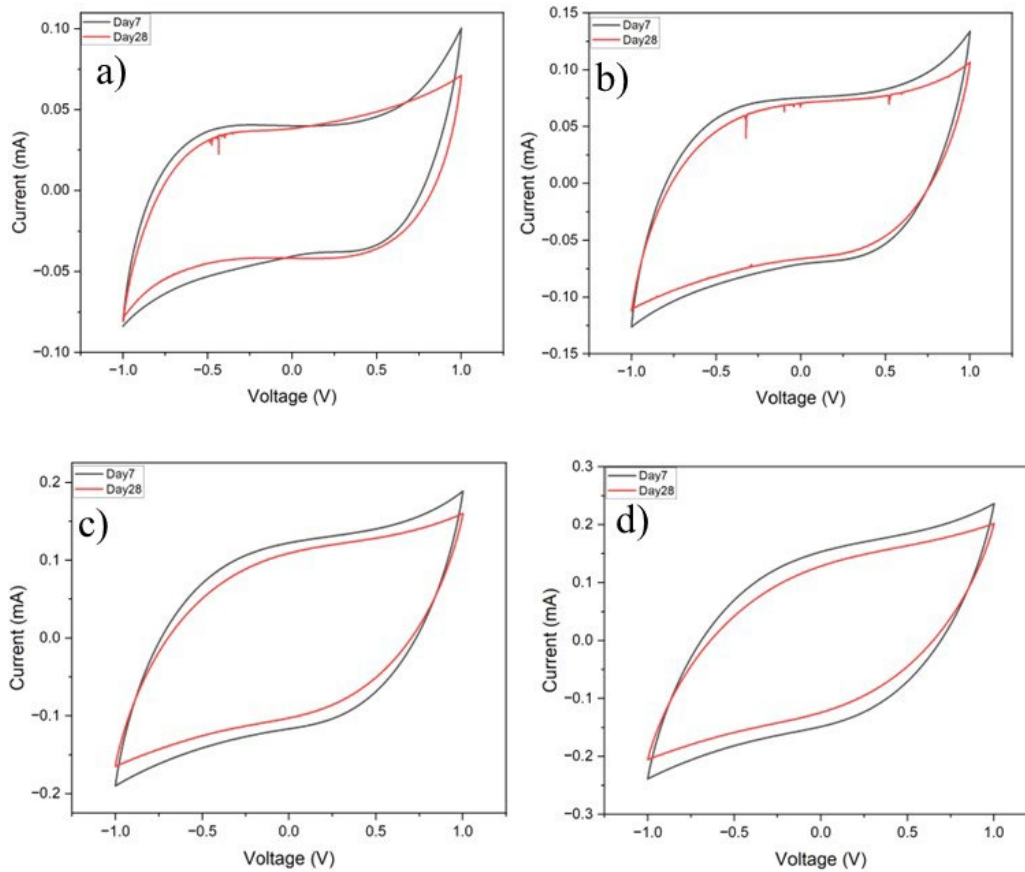
Figure 22. CV curves for the C-SW-SS composite at 7 and 28 days air curing using different scan rates. a) 50 mV/s, b) 100 mV/s, c) 200 mV/s, d) 300 mV/s.

Conclusions

For the first time, this paper investigates the electrochemical properties and multifunctional capabilities of a cementitious composite made with seawater and sea sand. The following conclusions are drawn:

1.   The experimental characterization coupled with DFT simulations demonstrated that, while the sea sand contains ionic K+ and Na+-bearing minerals, the activation energy barriers for these minerals are quite high, approximately 2.38 eV and 2.23 eV, respectively, rendering them less favorable for ionic conduction. Consequently, their contribution to the overall ionic conductivity of C-SW-SS is considered negligible.

2. The C-SW-SS composite exhibited higher C-S-H content compared to C-SW due to the positive effects of the sea sand on the cement hydration kinetics in the presence of sea water.

3. The amplified ion exchange between C-S-H and seawater, facilitated by the sea sand, resulted in C-SW-SS containing more Na^+, $Mg2^+$, and Cl^- ions compared to C-SW, with increases of approximately 17%, 50%, and 300%, respectively.

4. The enhanced ion exchange significantly reduced the ionic resistivity of C-SW-SS compared to C-SW, decreasing it from 165 kΩ·cm to 25 kΩ·cm. The C-SW-SS composite outperformed moist-cured conventional plain and conductively doped cementitious composites in terms of ionic resistivity. This improvement resulted in a higher ionic conductivity, placing it on par with solid-state electrolytes.

5. The C-SW-SS composite demonstrated exceptional sensitivity to low mechanical stress levels. This makes it uniquely suitable as a self-sensing structural health monitoring material to detect damage onset.

6. The C-SW-SS composite also exhibited promising electrochemical charge retention when cured in air for 28 days, highlighting potential for energy storage applications in concrete structures.

7. This work on C-SW-SS sets the stage for developing multifunctional cementitious composites for integration into sustainable and intelligent built environment.

8. Further research can build on these results by exploring compositional optimizations, small doping with conductive constituents, and processing methods to improve the ionic conductivity several folds higher towards industry needs.

9. With conductivity enhancement, the C-SW-SS composite can find broader applications in dams, roadways and buildings that simultaneously monitor their own structural health and store electrical energy through embedded cement cells.

724   10.   Further investigations are necessary to comprehensively understand the impact of

725   humidity variations on the self-sensing capabilities of the cementitious composite, as

726   the ionic conduction mechanisms and microstructural features may be susceptible to

727   moisture-induced changes. This could be crucial for ensuring long-term stability and

728   reliability of the self-sensing performance in various environmental conditions.

733 **References**

734 [1] Juenger, M. C. G., Winnefeld, F., Provis, J. L., & Ideker, J. H. (2011). Advances in
735 alternative cementitious binders. *Cement and Concrete Research* (Vol. 41, Issue 12, pp. 1232–
736 1243). https://doi.org/10.1016/j.cemconres.2010.11.012

737 [2] Hou, T.-C., & Lynch, J. P. (2005). Conductivity-based strain monitoring and damage
738 characterization of fiber reinforced cementitious structural components. *Smart Structures and*
739 *Materials 2005: Sensors and Smart Structures Technologies for Civil, Mechanical, and*
740 *Aerospace Systems*, *5765*, 419. https://doi.org/10.1117/12.599955

741 [3] Chen, P.-W., & Chung, D. D. L. (1993). Carbon fiber reinforced concrete for smart
742 structures capable of non-destructive flaw detection. *Smart Structures and Materials*, *2*, 22–
743 30. https://doi.org/10.1117/12.148502

744 [4] Wen, S., & Chung, D.D.L. (2000). Damage monitoring of cement paste by electrical
745 resistance measurement. *Cement and Concrete Research*, *30*(12), 1979–1982.
746 https://doi.org/10.1016/S0008-8846(00)00351-3

747 [5] Han, B., Ding, S., & Yu, X. (2015). Intrinsic self-sensing concrete and structures: A review.
748 *Measurement*, *59*, 110–128. https://doi.org/10.1016/j.measurement.2014.09.048

749 [6] D'Alessandro, A., Pisello, A. L., Sambuco, S., Ubertini, F., Asdrubali, F., Materazzi, A. L.,
750 & Cotana, F. (2016). Self-sensing and thermal energy experimental characterization of
751 multifunctional cement-matrix composites with carbon nano-inclusions. *Behavior and*
752 *Mechanics of Multifunctional Materials and Composites 2016*, *9800*, 98000Z.
753 https://doi.org/10.1117/12.2218680

[7] Mohseni, E., Tang, W., & Wang, S. (2019). Development of thermal energy storage lightweight structural cementitious composites by means of macro-encapsulated PCM. *Construction and Building Materials*, *225*, 182–195. https://doi.org/10.1016/j.conbuildmat.2019.07.136

[8] Saafi, M., Gullane, A., Huang, B., Sadeghi, H., Ye, J., & Sadeghi, F. (2018). Inherently multifunctional geopolymeric cementitious composite as electrical energy storage and self-sensing structural material. *Composite Structures*, *201*, 766–778. https://doi.org/10.1016/j.compstruct.2018.06.101

[9] Guan, H., Liu, S., Duan, Y., & Cheng, J. (2006). Cement based electromagnetic shielding and absorbing building materials. *Cement and Concrete Composites*, *28*(5), 468–474. https://doi.org/10.1016/j.cemconcomp.2005.12.004

[10] Galao, O., Bañón, L., Baeza, F. J., Carmona, J., & Garcés, P. (2016). Highly conductive carbon fiber reinforced concrete for icing prevention and curing. *Materials*, *9*(4). https://doi.org/10.3390/ma9040281

[11] Mccarter, W. J., Chrisp, T. M., Starrs, G., & Blewett, J. (2003). Characterization and monitoring of cement-based systems using intrinsic electrical property measurements. *Cement and Concrete Research*, *33*(2), 197–206. https://doi.org/https://doi.org/10.1016/S0008-8846(02)00824-4

[12] Sengul, O. (2014). Use of electrical resistivity as an indicator for durability. *Construction and Building Materials*, *73*, 434–441. https://doi.org/10.1016/j.conbuildmat.2014.09.077

[13] Li, G. Y., Wang, P. M., & Zhao, X. (2005). Mechanical behavior and microstructure of cement composites incorporating surface-treated multi-walled carbon nanotubes. *Carbon*, *43*(6), 1239–1245. https://doi.org/10.1016/j.carbon.2004.12.017

[14] Parveen, S., Rana, S., & Fangueiro, R. (2013). A review on nanomaterial dispersion, microstructure, and mechanical properties of carbon nanotube and nanofiber reinforced cementitious composites. In *Journal of Nanomaterials* (Vol. 2013). https://doi.org/10.1155/2013/710175

[15] Yu, H., Lei, Y., Pei, C., Wei, L., Zhu, J. H., & Xing, F. (2022). Enhancing the mechanical and functional performance of carbon fiber reinforced cement mortar by the inclusion of a cost-effective graphene nanofluid additive. *Cement and Concrete Composites*, *134*. https://doi.org/10.1016/j.cemconcomp.2022.104777

[16] Ji, X., Ge, Y., Li, M., Wang, L., & Liu, S. (2023). Preparation of carbon fiber conductive concrete and study on its mechanical and heating properties. *Journal of Materials Research and Technology*, *27*, 3029–3040. https://doi.org/10.1016/j.jmrt.2023.10.118

788 [17] Charitidis, C. A., Georgiou, P., Koklioti, M. A., Trompeta, A. F., & Markakis, V. (2014).
789 Manufacturing nanomaterials: From research to industry. *Manufacturing Review*, *1*.
790 https://doi.org/10.1051/mfreview/2014009

791 [18] Song, G., Gu, H., Mo, Y. L., Hsu, T. T. C., & Dhonde, H. (2007). Concrete structural
792 health monitoring using embedded piezoceramic transducers. *Smart Materials and Structures*,
793 *16*(4), 959–968. https://doi.org/10.1088/0964-1726/16/4/003

794 [19] Zhu, Y., Zhang, Z., Yao, Y., Guan, X., & Yang, Y. (2016). Effect of Water-Curing Time
795 on the Mechanical Properties of Engineered Cementitious Composites. *Journal of Materials in
796 Civil Engineering*, *28*(11). https://doi.org/10.1061/(asce)mt.1943-5533.0001636

797 [20] Chen, B., Wu, K., & Yao, W. (2004). Conductivity of carbon fiber reinforced cement-
798 based composites. *Cement and Concrete Composites*, *26*(4), 291–297.
799 https://doi.org/10.1016/S0958-9465(02)00138-5

800 [21] Wong, H. S., Pappas, A. M., Zimmerman, R. W., & Buenfeld, N. R. (2011). Effect of
801 entrained air voids on the microstructure and mass transport properties of concrete. *Cement
802 and Concrete Research*, *41*(10), 1067–1077. https://doi.org/10.1016/j.cemconres.2011.06.013

803 [22] D'Alessandro, A., Rallini, M., Ubertini, F., Materazzi, A. L., & Kenny, J. M. (2016).
804 Investigations on scalable fabrication procedures for self-sensing carbon nanotube cement-
805 matrix composites for SHM applications. *Cement and Concrete Composites*, *65*, 200–213.
806 https://doi.org/10.1016/j.cemconcomp.2015.11.001

807 [23] Han, B., Ding, S., & Yu, X. (2015). Intrinsic self-sensing concrete and structures: A
808 review. *Measurement*, *59*, 110–128. https://doi.org/10.1016/j.measurement.2014.09.048

809 [24] Li, P., Li, W., Yu, T., Qu, F., & Tam, V. W. Y. (2020). Investigation on early-age
810 hydration, mechanical properties and microstructure of seawater sea sand cement mortar.
811 *Construction and Building Materials*, *249*, 118776.
812 https://doi.org/10.1016/j.conbuildmat.2020.118776

813 [25] Xiao, J., Qiang, C., Nanni, A., & Zhang, K. (2017). Use of sea-sand and seawater in
814 concrete construction: Current status and future opportunities. *Construction and Building
815 Materials*, *155*, 1101–1111. https://doi.org/10.1016/j.conbuildmat.2017.08.130

816 [26] Dhondy, T., Remennikov, A., & Shiekh, M. N. (2019). Benefits of using sea sand and
817 seawater in concrete: a comprehensive review. In *Australian Journal of Structural Engineering*
818 (Vol. 20, Issue 4, pp. 280–289). https://doi.org/10.1080/13287982.2019.1659213

819 [27] Li, P., Li, W., Sun, Z., Shen, L., & Sheng, D. (2021). Development of sustainable concrete
820 incorporating seawater: A critical review on cement hydration, microstructure and mechanical
821 strength. *Cement and Concrete Composites*, *121*.
822 https://doi.org/10.1016/j.cemconcomp.2021.104100

823 [28] Belli, A., Mobili, A., Bellezze, T., & Tittarelli, F. (2020). Commercial and recycled
824 carbon/steel fibers for fiber-reinforced cement mortars with high electrical conductivity.
825 *Cement and Concrete Composites*, *109*. https://doi.org/10.1016/j.cemconcomp.2020.103569

826 [29]. Berkeley, L. (2024) The Materials Explorer open source software[EB/OL]. *The Materials*
827 *Project*, [2024-03-16].https://next-gen.materialsproject.org/

828 [30] Atkins, J.E. and McBride, E.F. (1992) Porosity and Packing of Holocene River, Dune, and
829 Beach Sands. *American Association of Petroleum Geologists Bulletin*, 76, 339-355.
830 https://doi.org/10.1306/BDFF87F4-1718-11D7-8645000102C1865D

831 [31] Curry, C. W., Bennett, R. H., Hulbert, M. H., Curry, K. J., & Faas, R. W. (2004).
832 Comparative study of sand porosity and a technique for determing porosity of undisturbed
833 marine sediment. *Marine Georesources and Geotechnology*, *22*(4), 231–252.
834 https://doi.org/10.1080/10641190490900844

835 [32] Evgenij Barsoukov, & J. Ross Macdonald. (2005). Impedance spectroscopy: theory,
836 experiment, and applications. *John Wiley & Sons, Inc*. https://doi.org/10.1002/0471716243

837 [33] Jonscher, A. (1977). The 'universal' dielectric response. *Nature*, *267*, 673–679.
838 https://doi.org/https://doi.org/10.1038/267673a0

839 [34] Zhao, Y., Hu, X., Shi, C., Zhang, Z., & Zhu, D. (2021). A review on seawater sea-sand
840 concrete: Mixture proportion, hydration, microstructure and properties. *Construction and*
841 *Building Materials*, *295*. https://doi.org/10.1016/j.conbuildmat.2021.123602

842 [35] Younis, A., Ebead, U., Suraneni, P., & Nanni, A. (2018). Fresh and hardened properties
843 of seawater-mixed concrete. *Construction and Building Materials*, *190*, 276–286.
844 https://doi.org/10.1016/j.conbuildmat.2018.09.126

845 [36] Ebead, U., Lau, D., Lollini, F., Nanni, A., Suraneni, P., & Yu, T. (2022). A review of
846 recent advances in the science and technology of seawater-mixed concrete. *Cement and*
847 *Concrete Research*, *152*. https://doi.org/10.1016/j.cemconres.2021.106666

848 [37] Sikora, P., Cendrowski, K., Abd Elrahman, M., Chung, S. Y., Mijowska, E., & Stephan,
849 D. (2020). The effects of seawater on the hydration, microstructure and strength development
850 of Portland cement pastes incorporating colloidal silica. *Applied Nanoscience (Switzerland)*,
851 *10*(8), 2627–2638. https://doi.org/10.1007/s13204-019-00993-8

852 [38] Bernard, E., Lothenbach, B., Le Goff, F., Pochard, I., & Dauzères, A. (2017). Effect of
853 magnesium on calcium silicate hydrate (C-S-H). *Cement and Concrete Research*, *97*, 61–72.
854 https://doi.org/10.1016/j.cemconres.2017.03.012

855 [39] Liu, W., Du, H., Li, Y., Yi, P., Luo, Y., Tang, L., & Xing, F. (2023). Effects of chloride
856 content on early hydration performance of cement pastes. *Materials Today Communications*,
857 *35*. https://doi.org/10.1016/j.mtcomm.2023.106257

858 [40] Randviir, E. P., & Banks, C. E. (2013). Electrochemical impedance spectroscopy: An
859 overview of bioanalytical applications. *Analytical Methods*, *5*(5), 1098–1115.
860 https://doi.org/10.1039/c3ay26476a

861 [41] Bisquert, J. (2002). Theory of the impedance of electron diffusion and recombination in a
862 thin layer. *Journal of Physical Chemistry B*, *106*(2), 325–333.
863 https://doi.org/10.1021/jp011941g

[42] Bockris, J. O., Reddy, A. K. N., & Gamboa-Aldeco, M. (2000). MODERN ELECTROCHEMISTRY Fundamentals of Electrodics (Vol. 2A). *Springer New York*. https://doi.org/https://doi.org/10.1007/b113922

[43] Zhao, C., Liu, L., Qi, X., Lu, Y., Wu, F., Zhao, J., Yu, Y., Hu, Y. S., & Chen, L. (2018). Solid-State Sodium Batteries. In *Advanced Energy Materials*. https://doi.org/10.1002/aenm.201703012

[44] Yoo, D.-Y.; You, I.; Lee, S.-J. Electrical Properties of Cement-Based Composites with Carbon Nanotubes, Graphene, and Graphite Nanofibers. Sensors 2017, 17, 1064. https://doi.org/10.3390/s17051064

[45] M. Jung, Y. -S. Lee and S. -G. Hong, "Effect of Incident Area Size on Estimation of EMI Shielding Effectiveness for Ultra-High Performance Concrete With Carbon Nanotubes," in IEEE Access, vol. 7, pp. 183105-183117, 2019, doi: 10.1109/ACCESS.2019.2958633.

[46] Seongwoo Gwon, Hyunjun Kim, Myoungsu Shin, Self-heating characteristics of electrically conductive cement composites with carbon black and carbon fiber, Cement and Concrete Composites, Volume 137,2023,104942, ISSN 0958-9465, https://doi.org/10.1016/j.cemconcomp.2023.104942.

[47] Wenkui Dong, Wengui Li, Guodong Long, Zhong Tao, Jianchun Li and Kejin Wang, Electrical resistivity and mechanical properties of cementitious composite incorporating conductive rubber fibres, Smart Mater. Struct. 28 085013, http://doi.org/10.1088/1361-665X/ab282a.